J. Fluid Mech. (2022), *vol*. 947, A19, doi:10.1017/jfm.2022.661

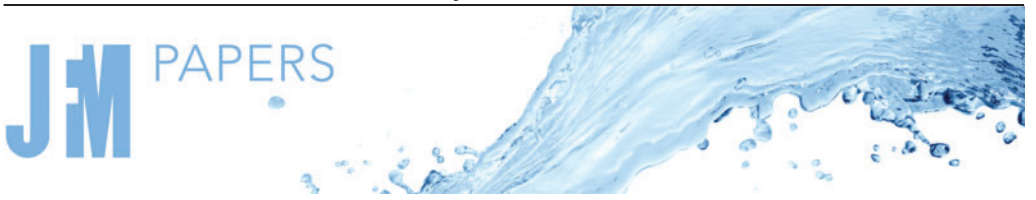

Turbulent separations beneath semi-submerged bluff bodies with smooth and rough undersurfaces

Xingjun Fang[1],†, **Mark F. Tachie**[1] **and Karen Dow**[2]

[1]Department of Mechanical Engineering, University of Manitoba, Winnipeg, MB R3T 5V6, Canada

[2]Department of Civil Engineering, University of Manitoba, Winnipeg, MB R3T 5V6, Canada

(Received 14 February 2022; revised 30 June 2022; accepted 27 July 2022)

The spatio-temporal characteristics of turbulent separations beneath semi-submerged bluff bodies with different undersurface roughness conditions are studied using a time-resolved particle image velocimetry. The Reynolds number based on the free-stream velocity and submergence depth was fixed to 14 400. Three different undersurface conditions – smooth, sandpaper roughness and cube roughness – were examined. The results showed that wall roughness reduces the mean reattachment length, and suppresses the Reynolds stresses in the second half of the mean separation bubble. The Kelvin–Helmholtz instability is observed at the leading edge of the smooth bluff body, but is bypassed in the rough cases. In the first half of the mean separation bubble, the frequencies in the separated shear layer migrate to lower values in a discrete manner through the vortex pairing mechanism. Consequently, multiple vortex shedding motions at different frequencies are nested in the separated shear layer, and the cores of shed vortices are aligned near the isopleth of free-stream velocity. The shed vortex is accompanied with multiple vortices along the edge of mean flow reversal in the upstream locations. These vortices are influenced significantly by wall roughness. A low-frequency flapping motion manifests as enlargement/shrinkage of reverse flow areas in the first half of the mean separation bubble. The frequencies of flapping motion in the smooth and sandpaper cases are similar, but are relatively lower than that in the cube roughness case. This flapping motion is associated with an extremely large vortex shed from the mean reattachment point to the free-stream region.

Key words: boundary layer separation

† Email address for correspondence: fangx@myumanitoba.ca

1. Introduction

Flow separations induced by two-dimensional sharp-edged bluff bodies in uniform flow as well as surface-mounted bluff bodies in the form of forward-facing or backward-facing steps immersed in a boundary layer have been studied extensively (Eaton & Johnston 1981; Hillier & Cherry 1981; Kiya & Sasaki 1983; Tafti & Vanka 1991; Pearson, Goulart & Ganapathisubramani 2013; Lander *et al.* 2016; Graziani *et al.* 2018; Moore, Letchford & Amitay 2019; Fang & Tachie 2020; Fang *et al.* 2021). For surface-mounted bluff bodies, the role of upstream wall roughness on the mean separation bubble, turbulent statistics and unsteady features of the separated shear layers has been examined critically in the recent past (Essel *et al.* 2015; Nematollahi & Tachie 2018; Fang & Tachie 2020). However, all these investigations have focused on hydrodynamically smooth bluff bodies even though two-dimensional bluff bodies with surface irregularities or roughness are common in diverse engineering and environmental applications. Typical examples include river flows around corroded bridge piers or beneath ice covers with irregular undersurfaces due to accumulation of debris. While considerable research on river ice covers, including pressure measurements (Coutermarsh & McGilvary 1993; Dow Ambtman, Steffler & Hicks 2011*b*) and stability analyses (Kivisild 1959; Uzuner & Kennedy 1972; Ashton 1974; Dow Ambtman, Steffler & Hicks 2011*a*), has been performed over the past decades, the ice covers were modelled using hydraulically smooth semi-submerged rectangular cylinders. This hinders an in-depth understanding of the effects of surface roughness on the fluid dynamics, and development of effective control strategy for realistic river ice processes. The present study is motivated by the need to understand the effects of roughness on the mean separated shear layer, Reynolds stresses and the unsteady characteristics of flow separations induced by bluff bodies.

For flow separations induced by rectangular bluff bodies subjected to incoming uniform flows, there exist two typical dominant instability mechanisms: Kelvin–Helmholtz (KH) instability and von Kármán (VK) vortex shedding. At the leading edge of a bluff body, the separated shear layer rolls up to form small-scale KH vortices. Behind the bluff body, VK vortex shedding occurs in the form of a train of alternating signed vortices that are convected in the downstream direction. Three distinct flow regimes can be identified based on the aspect ratio: (i) small aspect ratio, where the separated shear layer is shed directly into the wake region; (ii) intermediate aspect ratio, where the separated shear layer reattaches intermittently on the sidewall of the bluff body, but there exists an inherent interaction between the separated shear layer from the leading edge and the wake formed behind the bluff body; and (iii) large aspect ratio, where the separated shear layer reattaches permanently on the sidewall of the bluff body. The critical aspect ratios that demarcate the aforementioned regimes are not universal, due to a strong sensitivity of the flow dynamics to Reynolds number and incoming turbulence intensity. Based on the current literature, the critical aspect ratio demarcating the regimes of small and intermediate aspect ratios is between 2.0 and 3.5 (Okajima 1982; Nakagawa *et al.* 1998), whereas that demarcating the regimes of intermediate and large aspect ratios is larger than 5 (Moore *et al.* 2019; Kumahor & Tachie 2022).

Extensive research has been devoted to examine the unsteady characteristic of KH and VK instabilities, and their variation with aspect ratio and Reynolds number (which is defined as $Re_H = HU_\infty/\nu$, with H, U_∞ and ν being the bluff body height, incoming free-stream velocity and kinematic viscosity, respectively). The spatio-temporal characteristics of VK vortex shedding have been examined using proper orthogonal decomposition (POD). The vortex shedding motion manifests as a pair of POD modes, where the mode velocities are offset by a quarter wavelength, and the mode coefficients

have a shift of a quarter of phase (e.g. van Oudheusden *et al.* 2005; Legrand, Nogueira & Lecuona 2011). For a square cylinder, the Strouhal number $St_{VK} = f_{VK}H/U_\infty$, where f_{VK} is the frequency of VK vortex shedding in the wake region, is nearly constant at 0.13 for $Re_H > 1000$ (Okajima 1982; Durão, Heitor & Pereira 1988; Lyn & Rodi 1995; Brun *et al.* 2008; Bai & Alam 2018; Lander *et al.* 2018; Kumahor & Tachie 2022). For a fixed Reynolds number ($Re_H = 400$), Chiarini, Quadrio & Auteri (2022) observed that as aspect ratio increases, St_{VK} increases in a stepwise manner due to a phase-locking mechanism with the vortex shedding from the leading edge. Meanwhile, the Strouhal number $St_{KH} = f_{KH}H/U_\infty$, where f_{KH} is the frequency of KH instability, increases with Reynolds number according to $f_{KH}/f_{VK} = 0.18\,Re_H^{0.60}$ (Lander *et al.* 2018). For aspect ratios 2 and 3, there is a discontinuous variation of St_{VK} as Reynolds number increases (Okajima 1982). Moore *et al.* (2019) also observed that the manifestation of VK instability near the leading edge dominates the KH instability for aspect ratio 1, but is relatively weaker than the KH instability for aspect ratio 5. Overall, KH and VK instabilities interact with each other, and the underlying mechanisms vary with aspect ratio and Reynolds number.

In contrast to bluff bodies with small and intermediate aspect ratios, the KH instability near the leading edge of bluff bodies with large aspect ratios is not influenced by the VK vortex shedding in the wake region. As such, the separated shear layer exhibits dynamics drastically different to that of bluff bodies with short/intermediate aspect ratios. Experimental investigations by Ota and collaborators (Ota & Itasaka 1971; Ota & Narita 1978; Ota, Asano & Okawa 1981) examined the mean flow and Reynolds stresses within and downstream of the separation bubbles over a wide range of Reynolds numbers ($Re_H \in [40, 66\,600]$) using hot-wire. Their results demonstrated that the mean reattachment length (L_r) increases as the Reynolds number Re_H increases to 100–150, and then gradually decreases to an asymptotic value of approximately $9H$ as the Reynolds number increases further. Sasaki & Kiya (1991) observed a similar non-monotonic variation of L_r with Re_H, and also demonstrated that the vortex filaments in the separated shear layer undulate to form discrete hairpin-like structures in a staggered arrangement for $Re_H \in [380, 580]$. Using pointwise measurements of wall pressure and velocity as well as visualization techniques, Kiya & Sasaki (1983, 1985) and Cherry, Hillier & Latour (1984) investigated flow separation over a long plate in uniform flow at $Re_H = 26\,000$ and 32 000, respectively. They noted the co-existence of two distinct unsteady features: one associated with the quasi-periodic vortex shedding in the separated shear layer at frequency (0.5–0.6) U_∞/L_r, and the other associated with a low-frequency enlargement/shrinkage of the separation bubble (namely, flapping motion) at frequency (0.08–0.2) U_∞/L_r. Similar observations were also made by Tafti & Vanka (1991) for the flow separation over a long rectangular bluff body at a lower Reynolds number ($Re_H = 1000$). The flapping motion at a similar frequency was also reported for flow separations induced by a backward-facing step (Eaton & Johnston 1982), a forward–backward facing step (Chalmers, Fang & Tachie 2021), and adverse pressure gradient (Mohammed-Taifour & Weiss 2016).

Cimarelli, Leonforte & De Angeli (2018) conducted direct numerical simulations for flow separations induced by a rectangular bluff body of aspect ratio 5 at $Re_H = 3000$. They observed the transition from spanwise vortex filaments near the separating point to a hairpin-like structure after the reattachment point (which is in line with the experimental study of Sasaki & Kiya 1991) as well as the low-frequency flapping motion embracing the entire flow separation (which agrees with Kiya & Sasaki 1983, 1985). Cimarelli *et al.* (2018) concluded that the leading edge small-scale vortices and flapping motion form a self-sustaining cycle.

The effects of boundary layer thickness, Reynolds number and surface roughness conditions for incoming wall boundary layers on the statistical properties for the flow separations induced by a wide range of surface-mounted bluff bodies have been studied extensively (Piirto *et al.* 2003; Hattori & Nagano 2010; Sherry, Lo Jacono & Sheridan 2010; Essel & Tachie 2015, 2017; Hearst, Gomit & Ganapathisubramani 2016; Kumahor & Tachie 2022). It has been demonstrated that wall roughness upstream of a forward-facing step reduces the mean reattachment length over the step by 20–50 %. The interactions between the coherent structures embedded in the approaching wall boundary layers and flow separations have been investigated recently (Pearson *et al.* 2013; Fang & Tachie 2019*b*, 2020; Fang *et al.* 2021). The results of these studies demonstrated that the large-scale motion (Adrian, Meinhart & Tomkins 2000) and hairpin structures (Zhou *et al.* 1999) residing in wall boundary layers impose a quasi-periodic flapping motion at the same characteristic frequencies.

In a recent study (Fang *et al.* 2022), the authors performed a comprehensive experimental investigation of undersurface roughness, Reynolds number and Froude number on the mean flow and Reynolds stresses for turbulent flow separation beneath semi-submerged rectangular blocks. These blocks were employed to mimic river ice covers, following previous investigations on stability analysis (Kivisild 1959) and pressure measurements (Pariset & Hausser 1961; Dow Ambtman *et al.* 2011*a*) in the same context. The undersurface conditions consist of a reference hydraulically smooth surface and sandpaper roughness. The experiments were performed for a wide range of upstream velocities and submergence depth cumulating into 23 test conditions that facilitate a systematic investigation of undersurface roughness, Reynolds number, and Froude number on the mean reattachment length, as well as the mean velocity and Reynolds stresses. The objective of the present study is to investigate the effects of wall roughness on the spatio-temporal characteristics of vortical structures in the flow separation beneath semi-submerged bluff bodies using time-resolved particle image velocimetry (PIV). Particular attention is also paid to clarifying the role of wall roughness on the interactions of vortical structures originating from flow separation and the shear layer. The present analyses, exploiting the time-resolved PIV data for the smooth bluff body, also complement the structural mechanisms inferred from pointwise measurements by Kiya & Sasaki (1983, 1985).

The remainder of this paper is organized as follows. In § 2, the experimental facility, test cases and measurement procedure are detailed. In § 3, the experimental results are discussed in terms of turbulence statistics as well as the unsteady characteristics of separated shear layer and flow reversal. Finally, § 4 summarizes the major conclusions of this research.

2. Experimental set-up

The experiments were conducted in a recirculating open water channel in the Turbulence and Hydraulic Engineering Laboratory (THEL) at the University of Manitoba. The open water channel consists of a flow conditioning unit, a test section and a return plenum. The water flow is driven into the flow conditioning unit using a pump regulated by a 30 kW variable-speed drive motor before entering the test section. The flow conditioning unit consists of a perforated plate, a hexagonal honeycomb and mesh screens of different sizes, followed by a 4.88 : 1 converging section. The side and bottom walls of the test section are fabricated using Super Abrasion Resistant® transparent acrylic plates of 31.8 mm thickness, so as to allow optical access from all directions. The interior dimensions of

the test section are 6.00 m × 0.45m × 0.60 m in the streamwise, vertical and spanwise directions, respectively. The water flow exiting the test section enters the return plenum, where it is diverted by a turning vane system to a returning pipe and then goes back to the flow conditioning unit.

Figure 1 illustrates the side view of the experimental set-up and fields of view of the cameras of the PIV system, as well as the coordinate system and nomenclatures employed in the present research. A box (the blue area in the figure) spanning the entire water channel width was made of acrylic plates. Its streamwise length (L) and vertical height were 1.0 m and 0.1 m, respectively. This box was fitted with a vertical threaded rod at each corner, and the threaded rods were fastened by pairs of nuts to two horizontal bars mounted rigidly over the water channel. The submergence of the box into the free-surface water flow was adjusted accurately by lowering or raising the threaded rods. The undersurface of the box was attached to three interchangeable plates (the orange area in the figure) to achieve three different wall roughness conditions. The three interchangeable plates were a smooth 6 mm thick acrylic plate, a 6 mm thick acrylic plate with 16-grit sandpaper (see figure 1*b*) glued on the undersurface, and a 6 mm thick acrylic plate machined to have staggered cubes (see figure 1*c*) on the undersurface. The average height, standard deviation, skewness and kurtosis of the sandpaper roughness, measured using an SMZ800N optical stereo microscope, are 1.54 mm, 0.42 mm, 0.63 and 3.08, respectively (Nematollahi & Tachie 2018). The cube roughness elements, on the other hand, were distributed uniformly with centre-to-centre spacing 6.0 mm, and their side lengths were constant at 3.0 mm (see figure 1*c*). As such, the combination of sandpaper and cube roughness test cases encompasses irregular and regular roughness configurations of drastically different sizes. The interchangeable plates were painted with non-reflective black paint to minimize the surface reflection of the laser. For convenience in the discussion, hereinafter, the test cases with the undersurfaces of smooth acrylic plate, sandpaper and cube roughness are termed the smooth case, the sandpaper case, and the cube roughness case, respectively, while both the sandpaper and cube roughness cases are collectively referred to as the rough cases. The origins of the streamwise (x) and vertical (y) coordinates are defined at the leading edge of the smooth undersurface or the roughness crest plane of the rough undersurfaces.

The box in figure 1 was adjusted so that its submergence depth (h) was kept at 0.03 m (i.e. the incoming free surface is at $y = 0.03$ m) for all three test cases. As such, the effective aspect ratio of the semi-submerged bluff body (L/h) was 33.3. This aspect ratio is large enough to ensure permanent flow reattachment onto the undersurface, and to eliminate any influence of the wake region on the flow separation near the leading edge. The velocity of incoming free-surface flow (U_∞) was 0.48 m s^{-1}, while the kinematic viscosity of the water (ν) was 10^{-6} m^2 s^{-1} at the laboratory room temperature (20 °C). The Reynolds number ($Re_h = U_\infty h/\nu$) was 14 400. The turbulence intensity (defined as $\sqrt{\overline{u'u'}}/U_\infty$) at the entrance of the test section is 1.3 %. The incoming water depth (D) was maintained at 0.43 m, so that the Froude number ($Fr_D = U_\infty/\sqrt{gD}$) was 0.23, and this ensured that the free-surface wave upstream of the semi-submerged box was negligible. If the free surface is assumed to act as a free-slip boundary, then the effective body height equivalent to that subjected to a uniform flow was twice of the submergence depth, i.e. $H = 0.06$ m. Thus the equivalent Reynolds number Re_H was 28 800, which is close to 26 000 and 30 400, respectively, investigated by Kiya & Sasaki (1983, 1985) and Moore *et al.* (2019).

A planar time-resolved particle image velocimetry (TR-PIV) system was used to measure the velocity field at the channel mid-span beneath the bluff body. The water

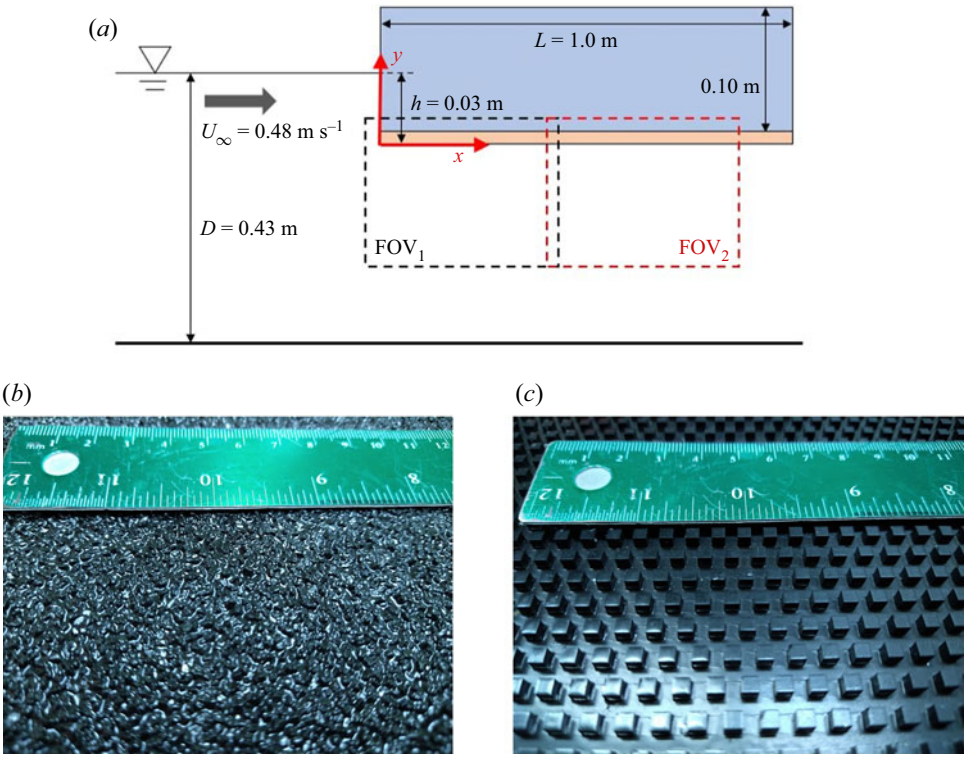

Figure 1. (*a*) Schematic of the experimental set-up (not to scale), the employed coordinate system, and fields of view (FOV_1 and FOV_2) of two cameras. Photos are shown of the (*b*) sandpaper and (*c*) cube roughness surfaces.

was seeded using 10 μm silver coated hollow glass spheres, whose specific gravity was 1.4. Following Raffel *et al.* (2007), the slip velocity (U_s) and relaxation time (τ_p) of the seeding particles are 2.2×10^{-5} m s^{-1} and 2.2×10^{-6} s, respectively (see Fang & Tachie 2019*b*). This slip velocity is orders of magnitude smaller than the measured velocity scales. Following Pope (2000), the smallest time scale in the flow (τ_η) is estimated according to $\tau_\eta/\tau_0 = Re_h^{-1/2}$ (where $\tau_0 \equiv h/U_\infty$ is the largest time scale in the flow), and its value is 5.2×10^{-4} s. Therefore, the present Stokes number of seeding particles ($S_k = \tau_p/\tau_\eta$) is 0.0042, which satisfies the recommendation $S_k \leqslant 0.05$ by Samimy & Lele (1991) for the velocities of seeding particles representing the instantaneous local velocities of the fluid. A diode-pumped dual-cavity dual-head high-speed Neodymium-doped yttrium lithium fluoride (Nd:YLF) laser (wavelength 527 nm) was positioned underneath the test section and shot vertically upwards at the channel mid-span to illuminate the seeding particles. Both cavities of the laser were fired simultaneously to deliver a total pulse energy 60 mJ pulse^{-1} at frequency 807 Hz. The particle images were captured by two high-speed 12-bit complementary metal oxide semiconductor (CMOS) cameras fitted with Nikon® 60 mm lenses at 807 Hz. The resolution of the cameras is 2560 pixel × 1600 pixel, and the pixel pitch of the image sensor is 10 μm. The particle image diameter was approximately 2–4 pixels to avoid the pixel-locking effect (Raffel *et al.* 2007). As illustrated in figure 1(*a*), two cameras were positioned side-by-side to capture the particle images in a large streamwise-vertical (*x*–*y*) plane beneath bluff bodies while maintaining a high-fidelity spatial resolution. The field of view of each camera was 192 mm and 123 mm in the

streamwise and vertical directions, respectively, and these two fields of view overlapped by approximately 15 mm in the streamwise direction.

A commercial software (DaVis version 10) supplied by LaVision Inc. (Michigan, USA) was used to control the TR-PIV system and acquire 60 000 particle images for each test case. This software was also employed to calculate the velocity vectors using a multi-pass cross-correlation algorithm parallelized in a graphics processing unit (GPU). The initial interrogation area was 128 pixel × 128 pixel with 50 % overlap, and the final interrogation area was 24 pixel × 24 pixel with 75 % overlap. The resulting vector spacing was 0.45 mm, so 67 velocity vectors cover one unit of submergence (h). The post-processing of velocity vectors was performed using in-house Matlab® scripts.

The measurement uncertainty of the present experimental data is assessed using the framework outlined by Sciacchitano & Wieneke (2016) and Essel, Tachie & Balachandar (2021). The measurement uncertainty percentages of the streamwise mean velocity (U), Reynolds normal stress ($\overline{u'u'}$ and $\overline{v'v'}$) and Reynolds shear stress ($\overline{u'v'}$) are, respectively, estimated as

$$\xi_U = \frac{Z_c}{U}\sqrt{\frac{\overline{u'u'}}{N_{eff}}}, \tag{2.1a}$$

$$\xi_{uu,vv} = Z_c\sqrt{\frac{2}{N_{eff}}}, \tag{2.1b}$$

$$\xi_{uv} = Z_c\sqrt{\frac{1+\rho_{uv}^2}{N_{eff}-1}}. \tag{2.1c}$$

In the above equations, $\rho_{uv} \equiv \overline{u'v'}/\sqrt{\overline{u'u'}\times\overline{v'v'}}$, $Z_c = 1.96$ and N_{eff} are, respectively, the correlation coefficient, the confidence coefficient for 95 % confidence, and the effective number of independent samples. With a time-resolved measurement over time duration T, N_{eff} is estimated as $N_{eff} \approx T/(2\tau)$, where τ is the integral time scale. Measurement uncertainties were calculated using (2.1a) at multiple points along the mean shear layers. The results indicate that the measurement uncertainties of the mean velocity, Reynolds normal stress and Reynolds shear stress are approximately 2 %, 8 % and 6 %, respectively, at a 95 % confidence level.

3. Results and discussion

3.1. *Turbulence statistics*

Figure 2 compares the contours of the streamwise mean velocity (U) among the three test cases. In the plots, the isopleths of $U = 0$ and the stream function $\Psi = 0$, where $\Psi(x, y = Y) \equiv \int_Y^0 U(x, y)\,\mathrm{d}y$, with Y representing the designated vertical location, are overlaid to facilitate visualization of the mean flow topology. The former encompasses the region of flow reversal, while the latter marks the mean separating streamline (Castro & Haque 1987; Mohammed-Taifour & Weiss 2016; Fang & Tachie 2019*b*). The isopleths of $U = 0$ and $\Psi = 0$ both start at the leading edge ($(x, y) = (0, 0)$) and intersect with the wall at the same point. This intersection point is the mean reattachment point beyond which the mean flow reattaches onto the undersurface, thus its streamwise distance from the leading edge defines the mean reattachment length L_r. The values of L_r in the smooth, sandpaper and cube roughness cases are 9.2h, 7.3h and 7.7h (or equivalently, 4.6H, 3.65H and

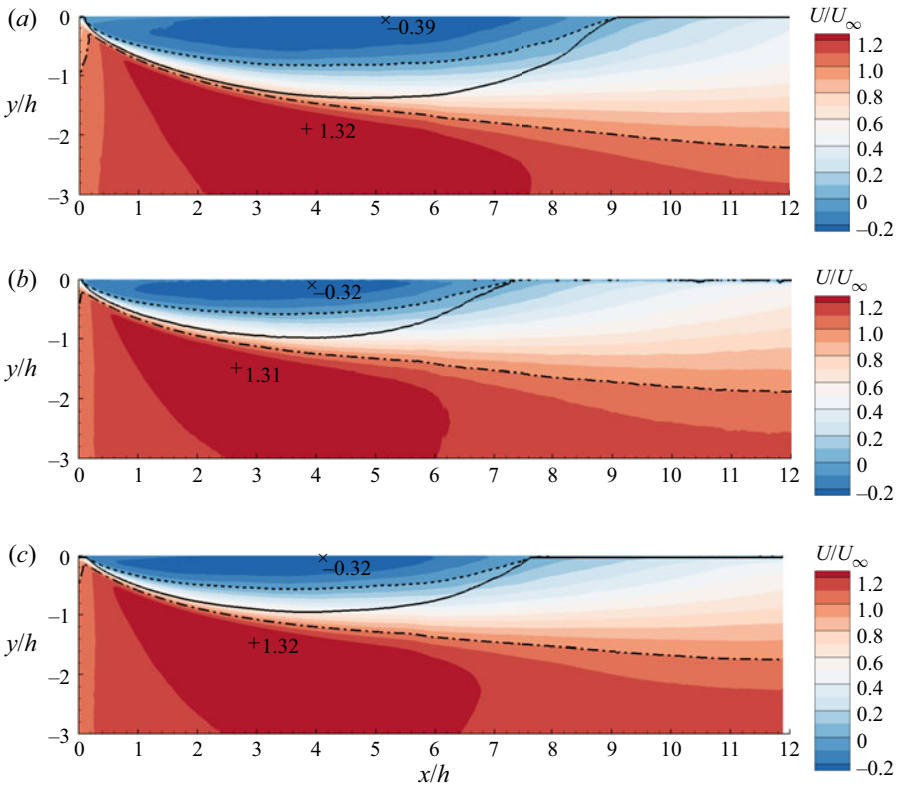

Figure 2. Contours of the streamwise mean velocity (U) for the (a) smooth, (b) sandpaper, and (c) cube roughness cases. The dashed, dash-dotted and solid isopleths are at $U = 0$, $U = U_\infty$ and $\Psi = 0$, respectively. Symbols + and × mark the locations of the maximum and minimum U, respectively, with the corresponding values written alongside.

3.85H), respectively. The present mean reattachment length ($L_r = 4.6H$) in the smooth case is in good agreement with 5.0H, 4.7H and 4.4H, respectively, reported by Kiya & Sasaki (1983), Djilali & Gartshore (1991) and Moore *et al.* (2019) for rectangular bluff bodies subjected to uniform incoming flows. This implies a similarity between the mean flow beneath a semi-submerged bluff body subjected to negligible free-surface waves, and that around bluff bodies in unbounded uniform flows.

From figure 2, the mean reattachment lengths in the rough cases are apparently shorter than that in the smooth case. It is also noted in figure 2 that a distinct mean shear layer emanating from the leading edge is flanked by regions of elevated streamwise mean velocity ($U > U_\infty$) and mean flow reversal ($U < 0$). The maximum values of U ($1.31U_\infty$–$1.32U_\infty$) are not altered significantly by the wall roughness, but the magnitude of the maximum mean flow reversal in the rough cases ($0.32U_\infty$) is 18 % smaller than that in the smooth case ($0.39U_\infty$).

Figure 3 compares the streamwise variation of the maximum Reynolds stresses in the vertical direction. In the region upstream of the bluff body, all Reynolds stresses retain their levels of the incoming free-stream turbulence state. This is a direct indication that with the present Froude number (0.23), free-surface waves neither alter the incoming turbulence level nor influence the flow separation beneath the semi-submerged bluff body. In the region of $x/h < 4$, the peak values of $\overline{u'u'}$ in the sandpaper case are generally

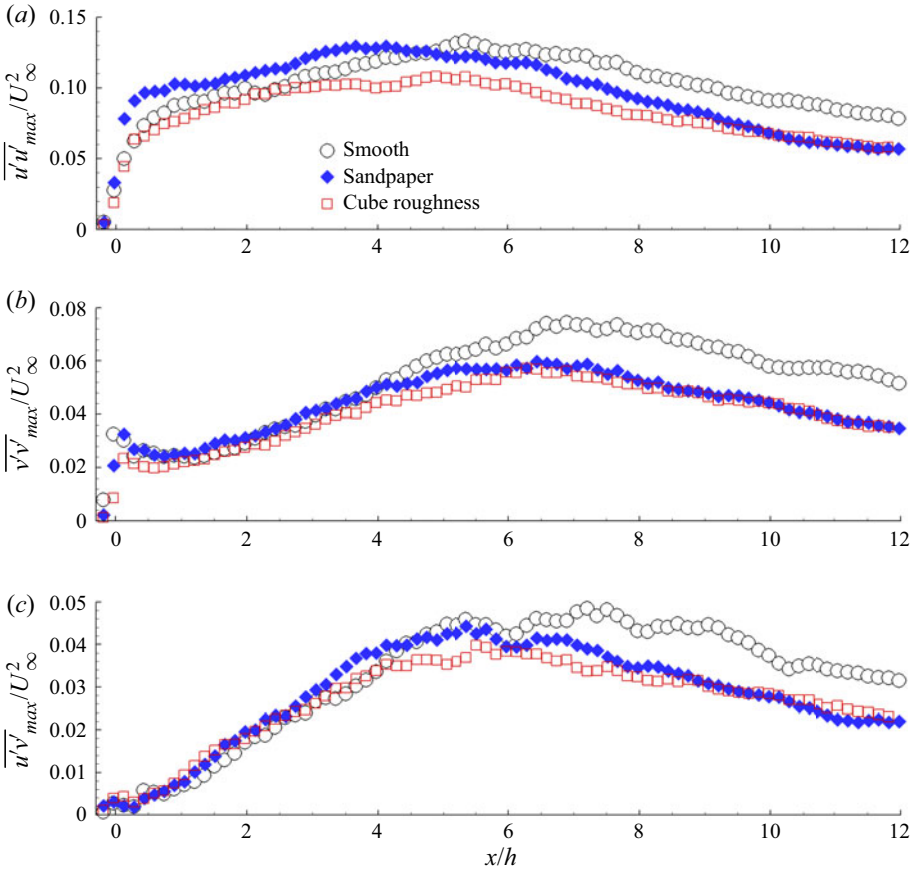

Figure 3. Streamwise variation of the maximum (*a*) $\overline{u'u'}$, (*b*) $\overline{v'v'}$ and (*c*) $\overline{u'v'}$ in the vertical direction. Every tenth measurement point is plotted for clarity.

higher than those in the other two cases, but the peak values of $\overline{v'v'}$ and $\overline{u'v'}$ in all cases are comparable. Turbulence transition near the leading edge is promoted by sandpaper, but not by the cube roughness. This underscores the difference between irregular and regular roughness types in the sandpaper and cube roughness cases. Compared with the rough cases, the smooth case possesses higher peak values of all three Reynolds stresses in the region $x \in [6, 12]$. It is also noted in figure 3 that the disparity observed in the Reynolds stresses for the sandpaper and cube roughness cases is most pronounced in the $\overline{u'u'}$ component for $x < 10$.

Following Moore *et al.* (2019), the averaged trajectory of the shear layer (denoted by Y_S) is defined as the vertical location of the maxima of the turbulence kinetic energy $E \equiv \frac{1}{2}(\overline{u'u'} + \overline{v'v'})$ (since the spanwise velocity was not measured). As presented in figure 4(*a*), the elevation of the mean shear layer away from the wall increases gradually in the first half of the mean separation bubble, and plateaus downstream of the centre of the mean separation bubble. This plateau is a manifestation of the trajectory of the separated shear layer diverging from the separating streamline in the second half of the mean separation bubble. This pattern is in line with the observations by Kiya & Sasaki (1983) and Moore *et al.* (2019). The asymptotic value of Y_S in the smooth case is in the

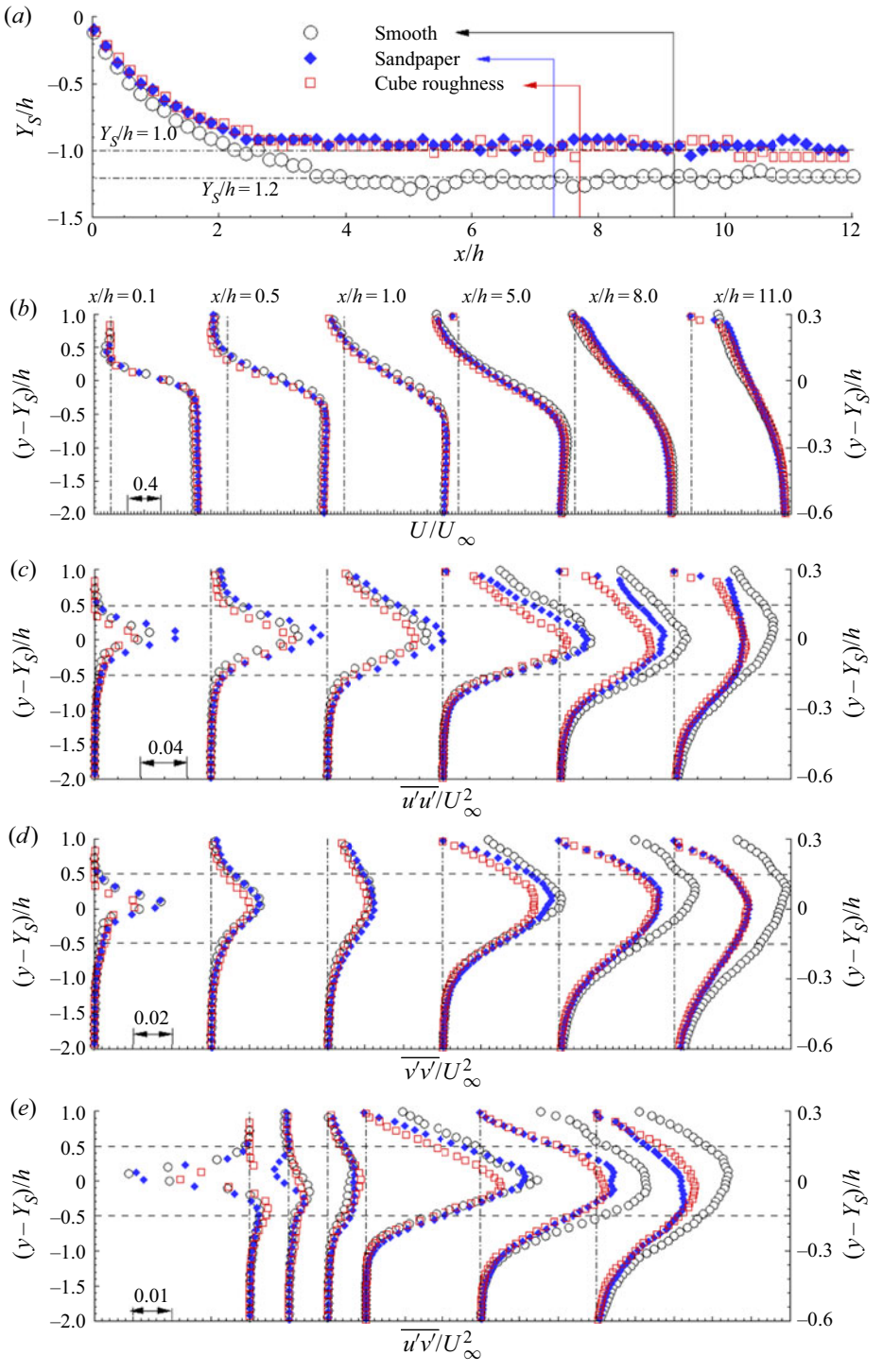

Figure 4. (*a*) Streamwise variation of the vertical centre of the mean shear layer (Y_S) (i.e. the peak elevation of $\frac{1}{2}(\overline{u'u'} + \overline{v'v'})$). Vertical profiles of (*b*) U, (*c*) $\overline{u'u'}$, (*d*) $\overline{v'v'}$, and (*e*) $\overline{u'v'}$, are plotted against $(y - Y_S)/h$. In (*a*), the vertical lines mark the mean reattachment lengths. In (*b–e*), the profiles of the first three streamwise locations use the vertical scale on the right, and the marked two horizontal dashed lines are symmetrical about $y = Y_S$. Not all measurement points are plotted, for clarity.

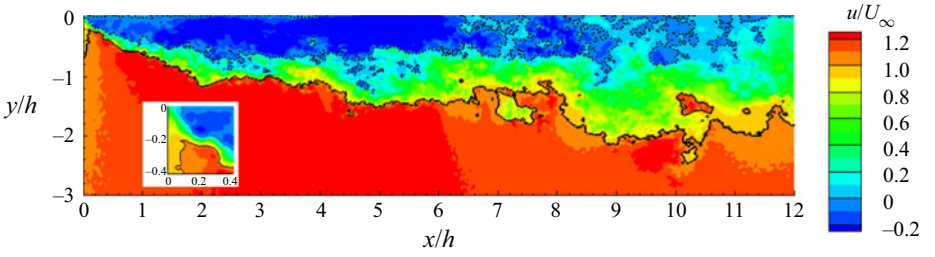

Figure 5. Contours of a typical instantaneous streamwise velocity (u) for the smooth case. The dashed and solid isopleths are at $u = 0$ and $u = U_\infty$, respectively. The inset magnifies the region near the leading edge.

range $(1.2 \pm 0.1)h$, which is in good agreement with values reported by Kiya & Sasaki (1983) and Moore *et al.* (2019). It is also observed that the variations of Y_S in both the sandpaper and cube roughness cases are almost indistinguishable, which is in line with the similar mean reattachment length observed for the rough cases in figure 2. For $x/h > 4$, the asymptotic values of Y_S for the smooth and rough cases are different by $0.2h$. This difference ($0.2h = 6$ mm) is apparently much larger than the roughness heights. The fact that wall roughness shifts the centre of the shear layer towards the wall by more than the roughness height is direct evidence that wall roughness significantly affects the turbulence structures within the separation bubble.

Figures 4(*b–e*) show the vertical profiles of mean velocity and Reynolds stresses at different streamwise locations. Note that the vertical coordinates are shifted by Y_S to facilitate comparison of flow statistics surrounding the separated shear layers in different cases. From figure 4(*b*), the profiles of streamwise mean velocity for all the test cases collapse well. It is therefore concluded that the streamwise mean velocity in the separated shear layer is not sensitive to the wall roughness. In contrast to the mean flow, the Reynolds stresses are susceptible to the wall roughness, as is shown evidently in figures 3 and 4(*c–e*). For instance, the peak magnitudes of the Reynolds stresses in the rough cases at $x/h = 11.0$ are almost 25 % smaller than those in the smooth case.

3.2. *Unsteadiness of the separated shear layer*

Figure 5 shows a typical example of the instantaneous streamwise velocity (u) field in the smooth case. Examples for the rough cases are qualitatively similar to figure 5, and therefore are not shown here for conciseness. The figure shows a distinct instantaneous shear layer emanating from the leading edge. This shear layer meanders as it evolves in the downstream direction, reflecting its unsteadiness. In this subsection, the unsteady characteristics of the separated shear layer and its sensitivity to different wall roughness conditions are elucidated.

3.2.1. *Shear layer interface*

In the context of the turbulent boundary layer (TBL), the mean shear is distributed across the entire boundary layer, but the instantaneous shear layers are concentrated at discrete wall-normal locations, creating the so-called uniform momentum zones in between (De Silva, Hutchins & Marusic 2016; De Silva *et al.* 2017). These instantaneous shear layers possess a constant streamwise velocity corresponding to local minima in the probability density function (p.d.f.) of the streamwise velocity (Adrian *et al.* 2000). The spatio-temporal and underlying structural mechanism of these instantaneous shear layers

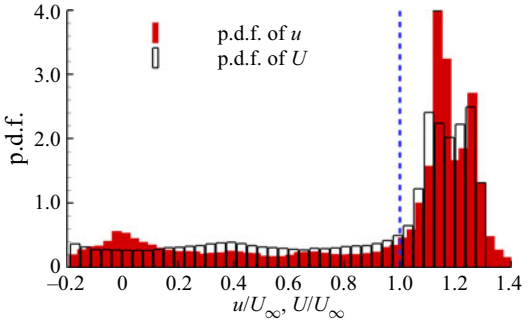

Figure 6. Probability density functions (p.d.f.s) of u in figure 5 and mean velocity U.

in the TBL have been studied extensively (Saxton-Fox & McKeon 2017; Laskari *et al.* 2018). As exemplified in figure 5, the instantaneous separated shear layer is apparent from visual inspection, and deserves a closer quantitative examination. To this end, the p.d.f. of the instantaneous streamwise velocity field for the same snapshot in figure 5(*a*) is examined in figure 6.

From figure 6, the p.d.f. of u exhibits a steep increase as it increases to values larger than U_∞, reflecting the near-uniform velocity in the region far away from the separated shear layer. On the other hand, the p.d.f. of u possesses a plateau at a low value for $u < U_\infty$. This suggests that primarily, the instantaneous shear layer is confined to the regions $u < U_\infty$. This shear layer is clearly different from the instantaneous internal shear layer embedded in the TBL. Specifically, the internal shear layer in the TBL features a narrow thickness on the order of a wall unit (De Silva *et al.* 2017), and is associated with a single velocity value corresponding to a local minimum in the p.d.f. of u. The geometry-induced shear layer in the present study features a thickness of the order of bluff body height, and therefore corresponds to a low-level plateau in the p.d.f. of u. It is deduced from figure 6 that the instantaneous shear layer is bounded by the isopleth of $u = U_\infty$. This deduction is consistent with the qualitative inspection in figure 5. Moreover, comparing the p.d.f.s of u and U in figure 6, the steep change in the p.d.f. at U_∞ persists in both the mean and instantaneous flow. This is indicative of the persistence of the shear layer interface defined by the isopleth of $u = U_\infty$. This deduction is reminiscent of the conclusion by Fang & Tachie (2019*a*) that the instantaneous shear layer induced by surface-mounted bluff bodies is bounded by the isopleth of the instantaneous streamwise velocity of the incoming flow at the bluff body height.

It should be noted that the above analysis is not applicable in the region very close to the leading edge (say $x/h < 0.1$). From the inset in figure 5, the isopleth of $u = U_\infty$ folds downwards, and does not well bound the shear layer close to the leading edge. In the following, investigation of the unsteadiness of the shear layer is limited to the region where $x/h > 0.1$. In figure 5, the isopleth of $u = U_\infty$ occasionally folds back onto itself to create enclosed 'islands' of low or high velocity, consistent with the topological characteristics of internal shear layer in the TBL (De Silva *et al.* 2017). As time evolves, these islands become connected to the long isopleth of $u = U_\infty$, while new islands appear. Therefore, most of these islands are likely representative of a two-dimensional slice of a three-dimensional isosurface of $u = U_\infty$, and should be counted as the shear layer region. Eventually, the interface bounding the instantaneous separated shear layer is defined as the outermost envelope of the isopleth of $u = U_\infty$. For convenience, this interface is hereinafter denoted by U^i_∞, and the vertical location is described using $y_e(x, t)$ which

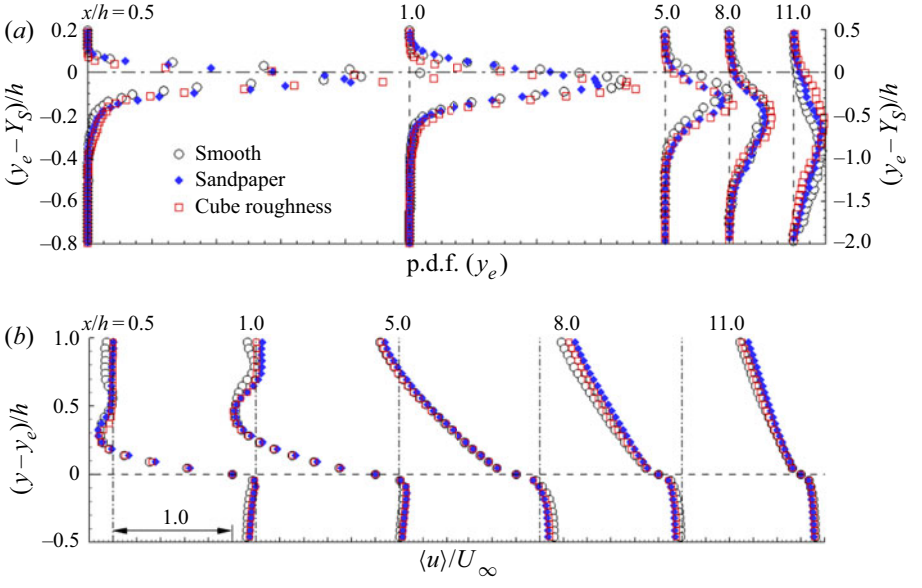

Figure 7. Vertical profiles of (*a*) the p.d.f. of y_e, and (*b*) the conditionally averaged streamwise velocity $\langle u\rangle$ across y_e, at selected streamwise locations. In (*a*), the profiles of the first three x/h use the scale on the left, while the other values use the scale on the right. Every third point is plotted, for clarity.

is a function of streamwise location x and time t. The space–time variation of y_e reflects the unsteady nature of the shear layer.

Following the techniques established for the analyses of interfacial layers in the TBL (De Silva *et al.* 2017) and jets (Westerweel *et al.* 2005), the p.d.f. of y_e and the conditional-averaged streamwise velocity (denoted by $\langle u\rangle$) in the vertical neighbourhood of instantaneous y_e at selected streamwise locations are examined. As seen in figure 7(*a*), the p.d.f. of y_e is skewed towards the locations of $y_e - Y_S < 0$, suggesting the frequent occurrence of U^i_∞ below the centre of the mean shear layer. The p.d.f. of y_e spans wider vertical ranges at locations further downstream, and remains fairly similar between different test cases. This suggests that the vertical location of the shear layer varies over a wider range in the downstream locations. This variation of vertical location of the shear layer is not affected strongly by the wall roughness. From figure 7(*b*), the vertical profile of $\langle u\rangle$ is representative of an approximated instantaneous shear layer, and remains similar for different test cases.

To further demonstrate the dynamic significance of U^i_∞ to the separated shear layer, the possibility of reconstructing the streamwise Reynolds normal stress by a convolution of the conditionally averaged shear layer $\langle u\rangle(y - y_e)$ with the p.d.f. of y_e is explored. This is expressed as

$$\langle u'u'\rangle(y) = \int_{-\infty}^{0} \langle u\rangle^2(y - y_e)\,\text{p.d.f.}(y_e)\,\mathrm{d}y_e - \left[\int_{-\infty}^{0} \langle u\rangle(y - y_e)\,\text{p.d.f.}(y_e)\,\mathrm{d}y_e\right]^2. \quad (3.1)$$

Figure 8 compares the reconstructed $\langle u'u'\rangle$ with the measured $\overline{u'u'}$ for different test cases. For the streamwise locations of $x/h = 0.5$ and 1.0, the reconstructed $\langle u'u'\rangle$ is in good agreement with $\overline{u'u'}$ except for the near-wall region. Evidently, the reconstruction of (3.1) only sensitizes vortices near the shear layer interface. The similarity of $\langle u'u'\rangle$ and $\overline{u'u'}$

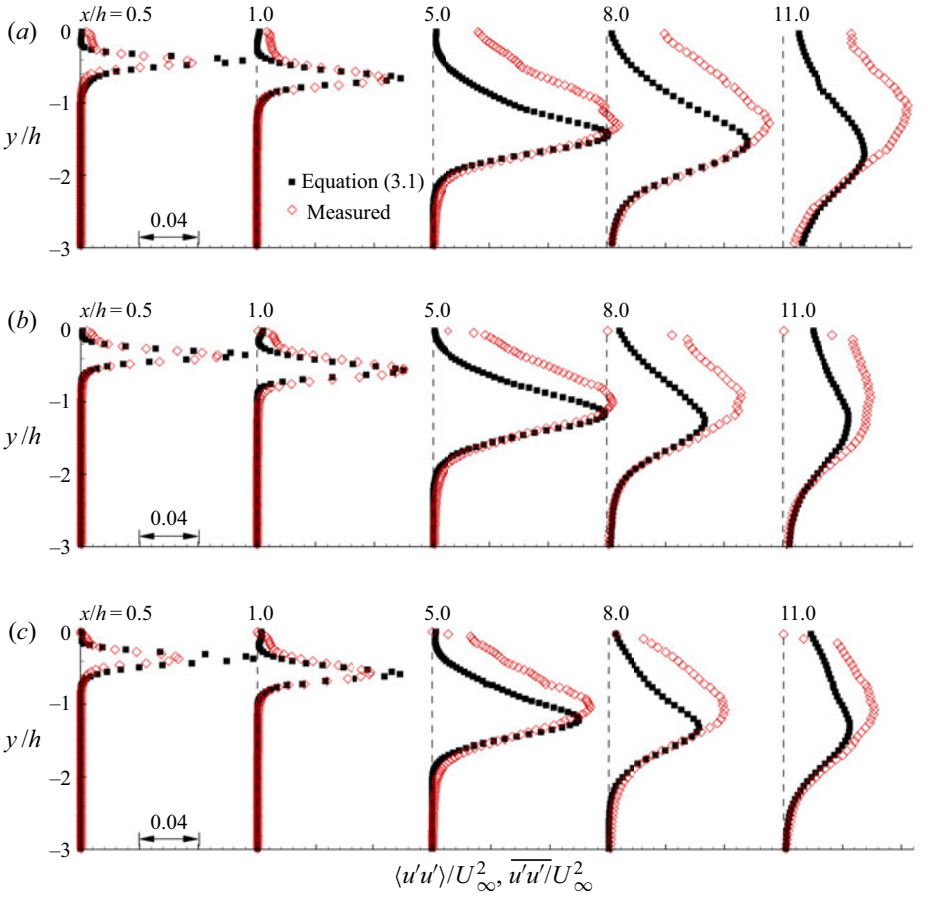

Figure 8. Vertical profiles of $\langle u'u' \rangle$ constructed from (3.1) and measured $\overline{u'u'}$ for the (*a*) smooth, (*b*) sandpaper, and (*c*) cube roughness cases. Not all grid points are plotted, for clarity.

for $x/h \leqslant 1.0$ is because the separated shear layer is not saturated with a wide range of length scales of vortices in the region of early turbulence transition. For $x/h \geqslant 5$, on the other hand, $\langle u'u' \rangle$ agrees well with $\overline{u'u'}$ below the peak location of $\overline{u'u'}$, but exhibits noticeable differences from $\overline{u'u'}$ between the peak location of $\overline{u'u'}$ and the wall. These differences emphasize the confinement effect of the wall on the development of the shear layer. For $x/h \geqslant 8.0$, the peak values of $\langle u'u' \rangle$ in the rough cases are smaller than those in the smooth case, which is consistent with the observation from $\overline{u'u'}$ in figures 3(*a*) and 4(*c*).

The temporal characteristics of the instantaneous shear layer interface U^i_∞ is investigated further using the frequency spectra of y_e at different streamwise locations. Note that the spectral analysis in the present study is implemented using Welch's overlapped window techniques (Welch 1967). The size and overlap of windows of Fourier transformation are 4.96 s (4000 snapshots) and 0.12 s (100 snapshots), respectively. As such, the resolved frequencies in the spectral analysis are multiples of $0.0126U_\infty/h$ (0.2018 Hz). For different test cases, as shown in figure 9, the oscillation of U^i_∞ downstream of the mean reattachment point is amplified at two distinct frequencies regardless of wall roughness conditions. These distinct frequencies observed in figure 9 are

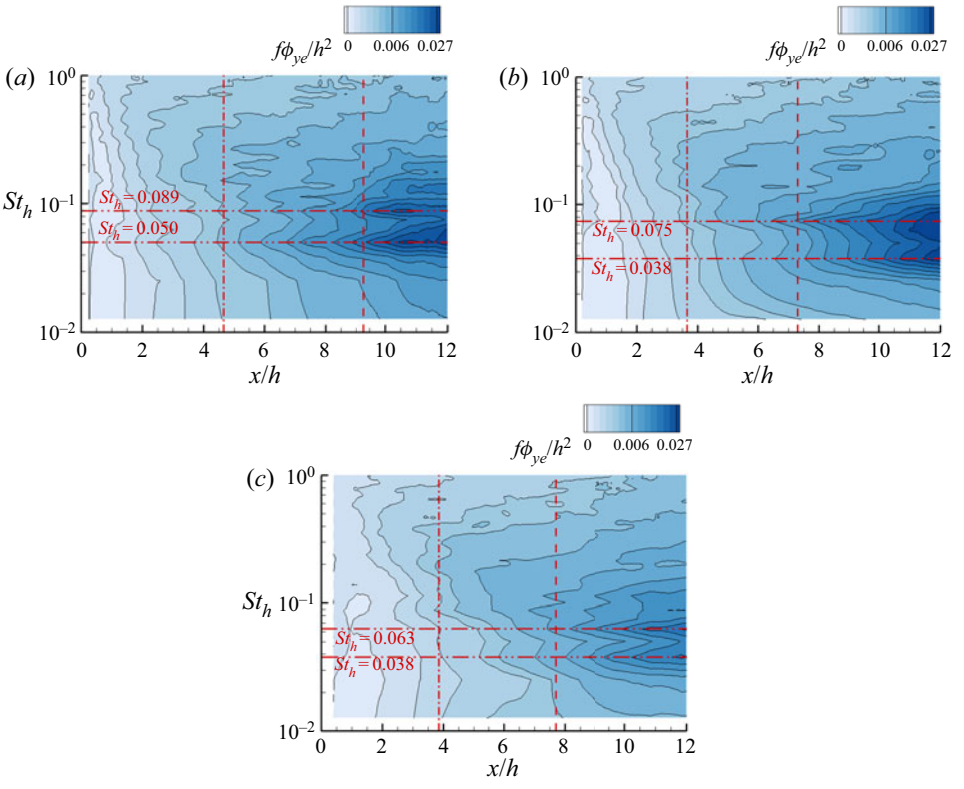

Figure 9. Premultiplied frequency spectra of y_e for the (*a*) smooth, (*b*) sandpaper, and (*c*) cube roughness cases. The horizontal dash-dot-dotted lines mark the characteristic frequencies, while the vertical dash-dotted and dashed lines mark, respectively, 50 % and 100 % of the mean reattachment length.

Mechanism (figure)	Smooth	Sandpaper	Cube roughness
Outermost bound (figure 9)	0.050*, 0.089	0.037, 0.075*	0.037, 0.063*
KH instability (figure 10)	3.6	–	–
Centre of mean shear layer (figure 11)	0.050*, 0.089, 0.115	0.025, 0.063*, 0.089	0.037, 0.094*
Near-wall u' (figure 12)	0.050, 0.089*	0.085*	0.094*
$A(t)$ in (3.2) (figure 14)	0.025*	0.025*	0.050*
The first SPOD modes (figure 15)	0.050*, 0.089, 0.115	0.063*, 0.115	0.037, 0.089*, 0.127

Table 1. Summary of significant Strouhal numbers (St_h) of different parameters/locations in different cases. Symbol – indicates non-existence, and superscript * marks the dominant Strouhal number.

summarized in table 1 along with other frequencies identified in the subsequent figures to facilitate comparison. It is interesting to note in figure 9 that for the smooth case, the significance of $St_h = 0.050$ is also visible in the first half of the mean separation bubble (see the local peak of the isopleth around $x/h \approx 1$). As for the rough cases, the significant frequencies identified downstream of the mean separation bubble do not manifest in the first half of the separation bubble. The underlying structural mechanism of these observations will be discussed in § 3.4.

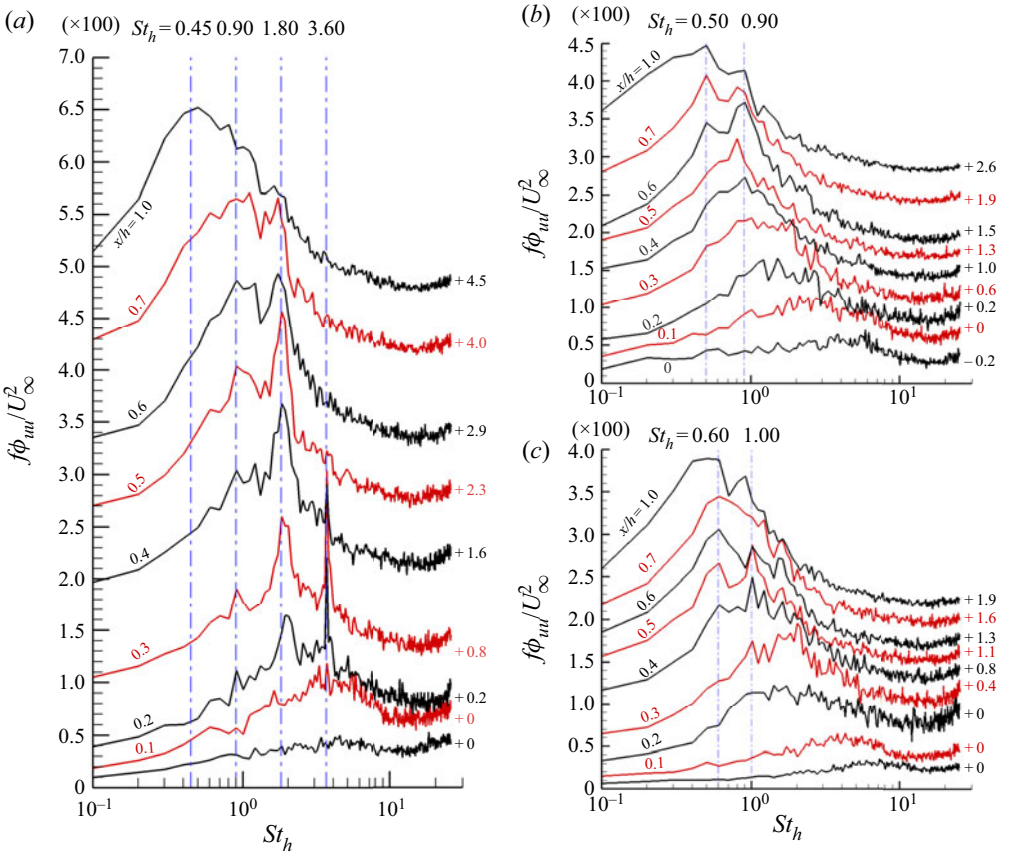

Figure 10. Premultiplied frequency spectrum of the streamwise velocity (ϕ_{uu}) at the streamwise locations $x/h = 0.0$, 0.1, 0.2, 0.3, 0.4, 0.5, 0.6, 0.7 and 1.0 along the peak locations of E (see figure 4*a*) for the (*a*) smooth, (*b*) sandpaper, and (*c*) cube roughness cases. To facilitate visualization, the spectra are vertically offset by the values indicated on the right-hand side. Vertical dash-dotted lines mark characteristic St_h numbers.

3.2.2. *Frequency migration*

Figure 10 presents the streamwise variation of frequency spectra of the streamwise fluctuating velocity (ϕ_{uu}) along the mean shear layer for different cases (see figure 4*a*). At the leading edge ($x/h = 0$), the spectra for all test cases are of low magnitudes and do not possess any dominant frequency. This is in contrast to the observation by Moore *et al.* (2019) that for rectangular cylinders of aspect ratios less than 5, the dominant frequency associated with the VK vortex shedding in the wake region also manifests at the leading edge. In the present study, the streamwise length of the bluff body is 33 times its effective height (submergence depth), so instantaneous flow reattachment over the undersurface of the bluff body is guaranteed to exclude any influence of wake flow dynamics on the separated shear layer at the leading edge. Overall, low-intensity white noise at the leading edge is imposed by the incoming flow condition, and the frequency spectra presented in figure 10 showcase the development of a separated shear layer subjected to different wall roughness conditions.

As seen in figure 10(*a*), slightly downstream of the leading edge at $x/h = 0.1$, a broad peak centred around Strouhal number St_h ($\equiv fh/U_\infty$) 3.60 appears. Further downstream, at $x/h = 0.2$, a sharp dominant peak at $St_h = 3.60$ becomes distinct, and is attributed to the

KH instability. This is in good agreement with the observation by Kiya & Sasaki (1983) that a dominant frequency $St_h \approx 3$ is induced by roll-up of the shear layer at $x/h = 0.2$ for a plate at a similar Reynolds number. In contrast to the present results, Moore *et al.* (2019) observed that the KH instability induced by a bluff body of aspect ratio 5 at a similar Reynolds number manifests as a broader peak of spectra around a similar frequency ($St_h \approx 4$), but it is closer to the leading edge (at $x/h = 0.046$). By comparing figures 10(*b*,*c*) with figure 10(*a*), in the two rough cases, sharp peaks of spectra do not occur near the leading edge, suggesting the bypass of KH instability.

It is also interesting to note in figure 10(*a*) that at $x/h = 0.2$, there exists a subdominant peak around the first sub-harmonic ($St_h = 1.80$) of the KH frequency. As x/h increases from 0.2 to 0.4, the magnitude (measured by $f\phi_{uu}$) of the sub-harmonic at $St_h = 1.80$ gradually dominates over the fundamental KH frequency, while the second sub-harmonic ($St_h = 0.90$) appears and strengthens. The spectral peak associated with the KH instability ceases to exist at $x/h = 0.5$. At locations further downstream, the dominance gradually switches from the first sub-harmonic ($St_h = 1.80$) to the second sub-harmonic ($St_h = 0.90$). At $x/h = 1.0$, the third sub-harmonic ($St_h = 0.45$) dominates while exhibiting a relatively broad peak. Based on the above observations, it is concluded that downstream of the leading edge in the separated shear layer, the dominant frequency decreases discretely through higher ranks of sub-harmonics, while the associated peak becomes broader. This pattern of frequency migration is due to the mechanism of vortex pairing occurring repeatedly. Specifically, small-scale spanwise vortices initiate because of the roll-up of the shear layer due to the KH instability around $x/h = 0.2$. Two adjacent vortices roll around each other as they are convected downstream, so as to form a single vortex of twice the size and half the frequency. This process repeats in the downstream direction leading to higher ranks of sub-harmonics of KH frequency. This repeating vortex pairing mechanism is well known to dictate the growth of the free shear layer (Winant & Browand 1974; Ho & Huerre 1984), and is evidently also at play for a separated shear layer.

From figures 10(*b*) and 10(*c*), a dominant frequency along with its sub-harmonic do not emerge until $x/h = 0.6$ and 0.4 for the sandpaper and cube roughness cases, respectively. Downstream of these locations, the dominance gradually shifts from the dominant frequency to its sub-harmonic, similar to the smooth case. This is a clear indication that the presence of wall roughness interrupts the vortex pairing mechanism near the leading edge, where the separated shear layer is close to the roughness elements. It is also emphasized that the migration from high to low frequency in the rough cases is slower than that in the smooth case. For instance, between $x/h = 0.4$ and 1.0, the dominant frequency decreases twofold from $St_h \approx 0.9$ to ≈ 0.5 in the rough cases, but it decreases fourfold from $St_h = 1.80$ to 0.45 in the smooth case.

Figure 11 characterizes the variation of $f\phi_{uu}$ along the mean shear layer over the entire measurement domain (see figure 4*a*). In general, high levels of $f\phi_{uu}$ appear in the form of horizontally aligned bands. This is attributed to vortices being convected in the downstream direction while maintaining their characteristic frequencies. As seen in figure 11, these horizontally aligned bands of $f\phi_{uu}$ appear at multiple discrete frequencies at any streamwise location, and the associated frequencies clearly migrate to lower frequencies in the first half of the mean separation bubble. This suggests the coexistence of vortex shedding at discrete frequencies through the vortex pairing mechanism exemplified in figure 10. It is important to note here that Moore *et al.* (2019) reported a continuous, as opposed to discrete, migration of dominant frequency from the KH frequency near the leading edge to the vortex shedding frequency in the wake region behind a bluff body of aspect ratio 5. This difference with the present result reflects the interruption of development of KH instability by the VK vortex shedding in the wake region.

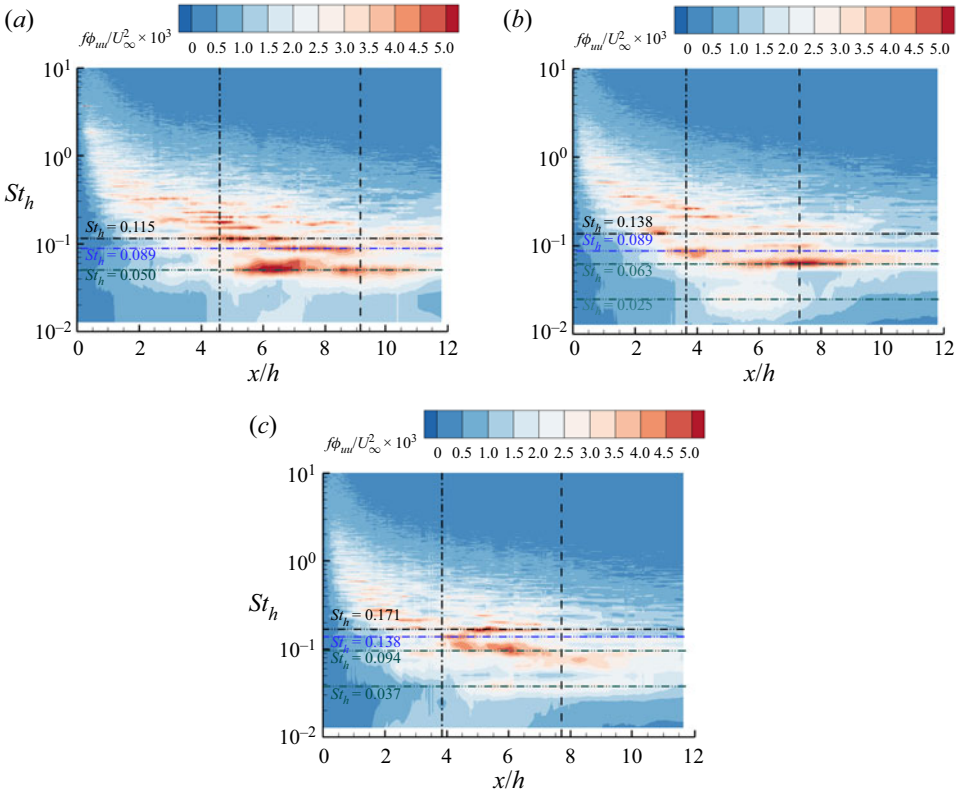

Figure 11. Variation of $f\phi_{uu}$ along the centre of the mean shear layer for the (*a*) smooth, (*b*) sandpaper, and (*c*) cube roughness cases. The vertical dash-dotted and dashed lines mark, respectively, 50 % and 100 % of the mean reattachment length. The horizontal dash-dot-dotted lines mark characteristic frequencies.

It is interesting to see in figure 11 that the migration to lower frequency ceases around the mid-point of the mean reattachment length. The dominance of multiple frequencies is maintained in the second half of the separation bubble. The underlying mechanism is explained as follows. In the first half of the mean separation bubble, the separated shear layer is relatively thin and gradually deflects away from the wall. As such, the larger vortices associated with lower frequencies occur through the vortex pairing mechanism. In the second half of the mean separation bubble, the distance of the separated shear layer from the wall remains constant (see figure 4*a*), so further vortex pairing is suppressed by the wall confinement. Consequently, vortices are shed downstream of the mid-point of the mean separation bubble while maintaining their characteristic frequencies.

It is shown in figure 11 that successive frequencies do not have to be the sub-harmonic of the predecessor fundamental frequencies. This suggests the occurrence of pairing between two vortices at different frequencies. Specifically, the pairing of two vortices at frequencies St_1 and St_2 (whose time scales are $1/St_1$ and $1/St_2$, respectively) generates a vortex at frequency $1/(1/St_1 + 1/St_2)$ (whose time scale is $1/St_1 + 1/St_2$). For instance, as seen in figure 11(*a*) for the smooth case, the significance of frequencies $St_1 = 0.115$, $St_2 = 0.089$ and $St_3 = 0.050$ is evident. Although the harmonic of St_3 at 0.100 is not discernible, St_3 is indeed $1/(1/St_1 + 1/St_2)$, suggesting that the vortices at $St = 0.050$ are generated by the pairing of vortices at $St = 0.115$ and vortices at $St = 0.089$. A close examination of the identified significant frequencies in figures 11(*b*) and 11(*c*) indicates

that the aforementioned vortex pairing mechanism for the smooth case is not valid for the rough cases. This is not surprising. Since the radius of vortices in the second half of the mean separation bubble is close to the height of the mean separation bubble, these vortices interact directly with the wall and therefore are more susceptible to wall roughness. In accordance with figures 10(*b*,*c*) and 11(*b*,*c*), the occurrence of vortex pairing in the rough wall cases is limited to a subrange in the first half of the mean separation bubble. Indeed, for the vortex pairing to occur, the separated shear layer needs to be sufficiently far away from the wall, and the vortices need to be sufficiently small to avoid direct interaction with the wall.

In figure 11(*a*), the dominance of $St_h = 0.050$ in the smooth case is apparent. This frequency is similar to the vortex shedding frequencies ($St_h = 0.05 \sim 0.06$) observed by Kiya & Sasaki (1983) and Moore *et al.* (2019). From figure 11(*b*), the dominant frequency in the sandpaper case is $St_h = 0.63$, and its dominance does not persist beyond the mean reattachment point. As for the cube roughness case, the dominance of a particular frequency is less pronounced than the other two cases, and is at best identified to be between $St_h = 0.094$ and $St_h = 0.171$. This suggests a strong disruption of regular vortex shedding by the cube roughness. It is also noted in figure 11 that there exists a less prominent but clearly identifiable frequency ($St_h = 0.025$ and 0.037 in the sandpaper and cube roughness cases, respectively), lower than the dominant frequency in the smooth case. The interruption of vortex shedding/pairing by the wall roughness in the second half of the separation is responsible for the weaker Reynolds stresses than in the smooth case in the region of $x/h > 5$ (see figure 3).

3.3. *Unsteadiness of flow separation*

Attention is now turned to the unsteady characteristics of flow separation. Figure 12 compares the premultiplied frequency spectra $f\phi_{uu}$ at $y/h = -0.09$ for different test cases. This is inspired by Kiya & Sasaki (1985) who measured the unsteady velocity at $0.05h$ away from the wall to investigate the reverse-flow unsteadiness. As seen in figure 12(*a*) for the smooth case, the dominance of $St_h = 0.089$ initiates around the mean reattachment point and persists in the downstream direction. This dominant frequency is close to $St_h = 0.081$ observed by Kiya & Sasaki (1985). In accordance with table 1, the dominant frequency $St_h = 0.050$ in the mean shear layer becomes subdominant in the near-wall region around the mean reattachment point. Kiya & Sasaki (1985) also noted the disparity between the dominant frequencies in the shear layer and flow reversal around the mean reattachment point, and interpreted this disparity as 'dispersion of the large-scale vortices in strength and position'. In accordance with figures 12(*a*), 11(*a*) and 9(*a*), the vortex shedding motion at $St_h = 0.089$ is closer to the wall than that at $St_h = 0.050$. As such, the former is more influential in the near-wall region around the mean reattachment point while the later is more influential in the shear layer interface. By comparing figures 11(*b*) and 12(*b*) for the sandpaper case, the subdominant frequency $St_h = 0.089$ in the mean shear layer becomes dominant in the near-wall region, whereas the dominance of $St_h = 0.063$ observed in the mean shear layer is discernible in the near-wall region. As for the cube roughness case, based on figures 11(*c*) and 12(*c*), the dominance of $St_h = 0.094$ persists in the mean shear layer and in the near-wall region.

It is also worthwhile comparing the results in figure 12 with Cimarelli *et al.* (2018) on a DNS study of flow separation around a bluff body with aspect ratio 5 at a Reynolds number ($Re_h = 1500$ based on half of body height) one-tenth of the present study.

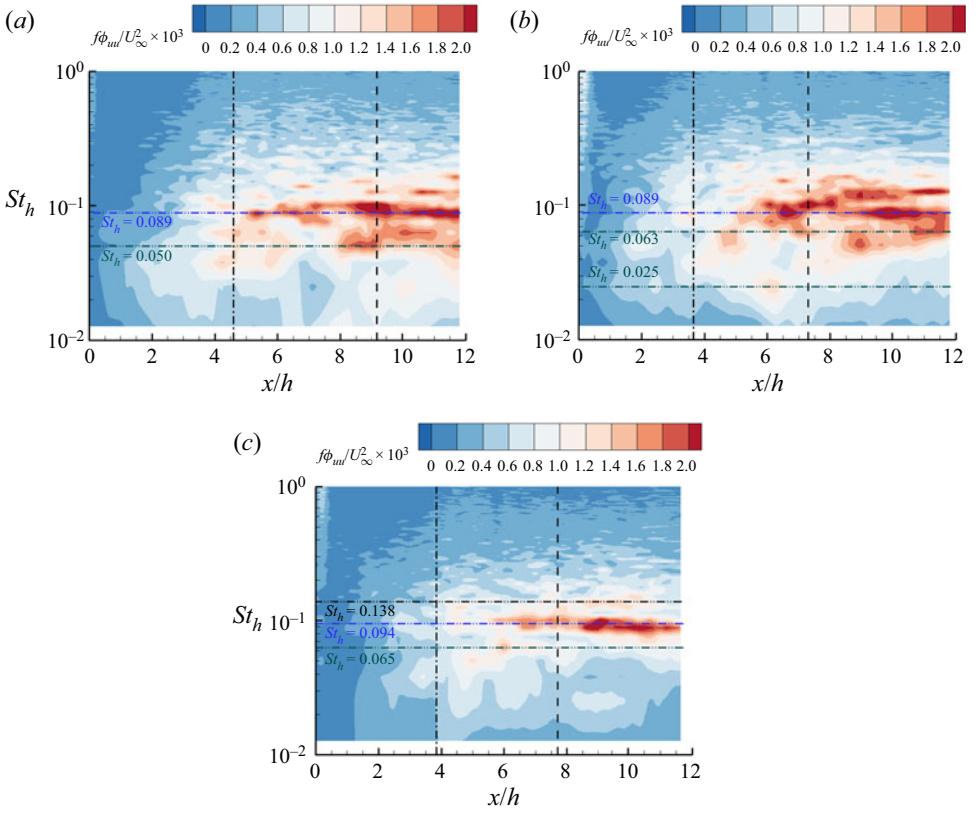

Figure 12. Streamwise variation of $f\phi_{uu}$ at $y/h = -0.09$ for the (*a*) smooth, (*b*) sandpaper, and (*c*) cube roughness cases. The vertical dash-dotted and dashed lines mark, respectively, 50 % and 100 % of the mean reattachment length. The horizontal dash-dot-dotted lines mark characteristic frequencies.

Cimarelli *et al.* (2018) examined the variation of dominant time scales (reciprocal of frequencies) along a near-wall mean streamline traced back near the mean reattachment point. The near-wall mean streamline of the present study is at a constant vertical elevation except for the regions close to the separating and reattaching points. This allows a direct comparison with the statistics along near-wall mean streamlines in Cimarelli *et al.* (2018). Specifically, Cimarelli *et al.* (2018) showed that the time scale in the near-wall region of the second half of the mean separation bubble is similar to that in the shear layer, which is consistent with the present observations from figures 11(*a*) and 12(*a*). Cimarelli *et al.* (2018) also observed that as the separating point is approached along the near-wall mean streamline, the time scale gradually increases in the first half of the mean separation bubble. This is in sharp contrast to the present results. As seen in figure 12, regardless of the wall roughness condition, the dominant frequencies exhibit an abrupt change near the middle point of the mean reattachment length. This disparity with Cimarelli *et al.* (2018) is due to the differences in Reynolds number and aspect ratio of bluff bodies.

In Kiya & Sasaki (1983) and Moore *et al.* (2019), the integral time scales from their pointwise measurements at various locations of the flow separation bubble were analysed. In the present study, whole-field time-resolved velocity data are exploited to investigate the time scales of the entire separation bubble. Here, the integral time scale (τ) is calculated by integrating the temporal autocorrelation of u' from the time displacement of zero to the

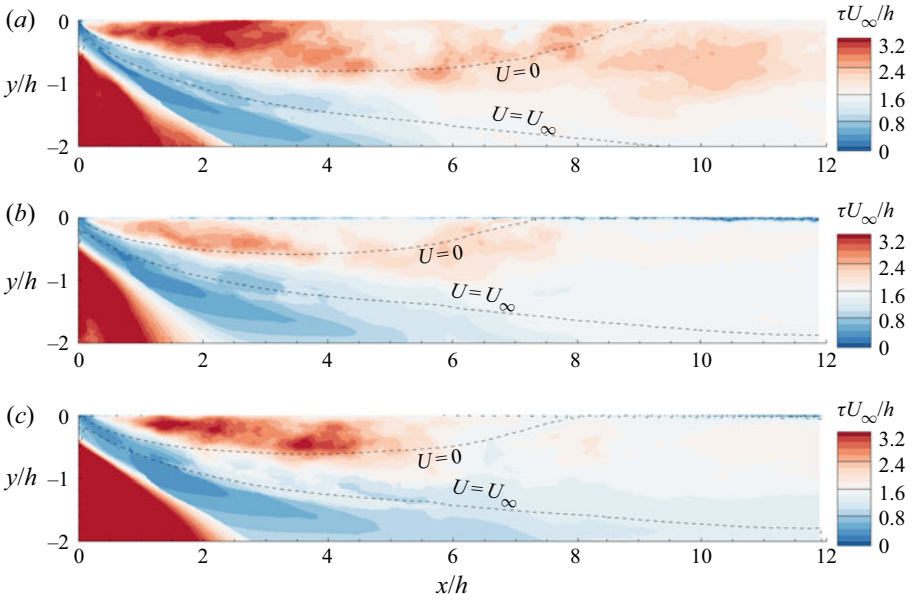

Figure 13. Contours of the integral time scales τ for the (*a*) smooth, (*b*) sandpaper, and (*c*) cube roughness cases.

point associated with the first zero correlation, and the results are presented in figure 13. Outside the mean separation bubble (see the lower left corners of the plots), the high values of integral time scales are associated with incoming turbulence, and are not of particular importance. It is, however, worth noting that along the mean separated shear layer, the values of the integral time scale generally increase in the downstream direction, and are of the order of h/U_∞ near the mean reattachment point. These are similar to the observations made by Kiya & Sasaki (1983) and Moore *et al.* (2019). In the near-wall region, on the other hand, the values of integral time scale tend to decrease in the downstream direction. In particular, there exists a distinct region of elevated integral time scale in the first half of the mean reverse flow area, where the streamwise Reynolds normal stress, $\overline{u'u'}$, is also significant (see figure 4*b*). These patterns of integral time scale in the near-wall region are persistent irrespective of the wall roughness condition. It is noted that the peak levels of the integral time scale in the first half of the mean reverse flow area for the sandpaper case are lower than those for the other two cases.

The observations from figures 12 and 13 suggest the existence of low-frequency motion residing exclusively in the first half of the mean separation bubble. This is reminiscent of the low-frequency flapping motion commonly observed in turbulent separation bubbles (Eaton & Johnston 1982; Kiya & Sasaki 1983; Cherry *et al.* 1984; Tafti & Vanka 1991; Cimarelli *et al.* 2018). Kiya & Sasaki (1983, 1985) noted the existence of a peak frequency between $St_h = 0.012$ and $St_h = 0.02$ at $x/L_r = 0.2$. Kiya & Sasaki (1985) presented the conditional-averaged streamwise velocity based on the surface pressure at $x/L_r = 0.2$, and observed that this low-frequency pressure is associated with vertical flapping (hence the term 'flapping motion') of the shear layer along with the thickening/thinning of flow reversal. Prompted by the results from figure 13 and results from Kiya & Sasaki (1983, 1985), the frequency spectra of the reverse flow area in the first half of the mean separation

bubble are further examined, and expressed as

$$A(t) = \int_{-\infty}^{0} \int_{0}^{0.5L_r} \mathcal{H}[u(x, y, t)]\, \mathrm{d}x\, \mathrm{d}y. \tag{3.2}$$

Here, $\mathcal{H}[u(x, y, t)]$ is 0 and 1 for positive- and negative-valued $u(x, y, t)$, respectively. Note that the integral range of x is between 0 and $0.5L_r$. It is noted that the above equation with an integral range of x over the entire measurement domain has also been evaluated, and the results are not as meaningful as those evaluated within $0 \leqslant x \leqslant 0.5L_r$.

Figure 14 compares the premultiplied frequency spectra of $A(t)$ for different test cases. The dominant frequency at $St_h = 0.025$ is evident for the smooth case. This frequency is close to the frequency of flapping motion of separation bubbles reported commonly in the literature (Eaton & Johnston 1982; Kiya & Sasaki 1983; Cherry *et al.* 1984; Tafti & Vanka 1991; Cimarelli *et al.* 2018). It is therefore concluded that the reverse flow area in the first half of the mean separation bubble exhibits a low-frequency sequence of enlargement and shrinkage. Cimarelli *et al.* (2018) also argued that the low-frequency flapping motion is 'strictly related to the behaviour of the secondary vortex', which occurs in the first half of the primary mean separation bubble. This confinement of low-frequency flapping motion to the first half of the mean separation bubble marks a significant difference between the flapping motions of separation bubbles induced by bluff bodies in uniform flow and those induced by surface-mounted bluff bodies subjected to incoming TBL investigated by Pearson *et al.* (2013), Fang & Tachie (2019*b*, 2020) and Fang *et al.* (2021). For instance, Fang *et al.* (2021) reported that the reverse flow area of the entire separation bubble over a forward-facing step (FFS) in a turbulent channel flow experiences quasi-periodic expansion/contraction at multiple frequencies. These frequencies coincide with the fundamental and harmonic frequencies of incoming hairpin structures, but are significantly different from the typical frequencies of flapping motion due to development of separation shear layers (Eaton & Johnston 1982; Kiya & Sasaki 1983; Cherry *et al.* 1984; Tafti & Vanka 1991; Cimarelli *et al.* 2018). Fang & Tachie (2019*b*) and Fang *et al.* (2022) demonstrated that the dominant frequencies of reverse flow areas reflect the interaction of incoming large-scale motion (Adrian *et al.* 2000) and hairpin structures with the FFS. For example, Fang *et al.* (2022) showed that as a hairpin structure is leaning over the step, it induces a pair of vertical counter-rotating vortices on the frontal surface, while an opposite-signed pair of counter-rotating vortices forms near the wall over the step. As a consequence, an enlarged reverse flow area upstream of the step is typically associated with a reduced reverse flow area over the step. In the present study, however, the incoming flow is of low turbulence intensity, and turbulence transition occurs only downstream of the leading edge. As such, the flapping motion of flow separation reflects the interaction of vortical structures originating in the shear layer with flow reversal, which will be clarified in the next subsection. It is worth noting in figure 14 that the dominant frequency of reverse flow area in the first half of the mean separation bubble for the sandpaper case is the same ($St_h = 0.025$) as that in the smooth case, whereas that in the cube roughness case is at a relatively higher value, i.e. $St_h = 0.050$.

3.4. *Spectral proper orthogonal decomposition analysis*

Thus far, it has been demonstrated that the incoming free-surface flow is effectively a free-slip boundary, so the present smooth case exhibits many similarities with the turbulent separations induced by a bluff body exposed to incoming uniform flows (Kiya & Sasaki 1983, 1985). To identify the dominant frequencies along with their associated vortical

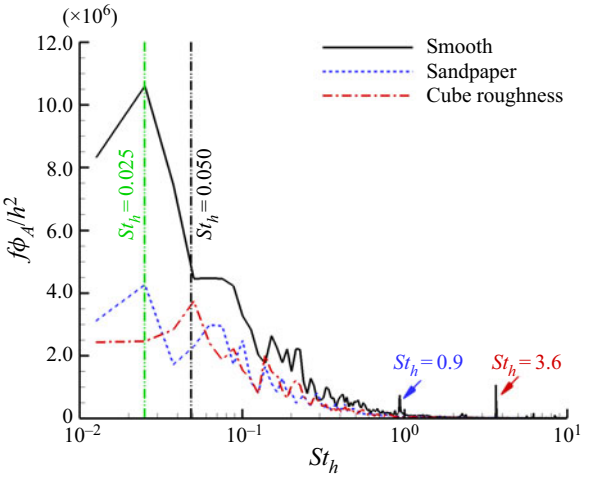

Figure 14. Premultiplied frequency spectra of reverse flow area ($f\Phi_A$) in the first half of the mean reattachment length.

structures, Kiya & Sasaki (1983, 1985) used statistical techniques such as conditional average, frequency filtering and auto/cross-correlation to analyse pointwise measurement data of velocity and wall pressure. In this subsection, an investigation of both the spatial and temporal characteristics of the pertinent vortical structures is conducted to exploit fully the time-resolved whole-field measurements using spectral proper orthogonal decomposition (SPOD) (Towne, Schmidt & Colonius 2018).

In the framework of SPOD, the fluctuating velocity field is decomposed into different modes at different frequencies as follows:

$$\boldsymbol{u}'(\boldsymbol{X}, t) = \sum_{j=1}^{\infty} \hat{\boldsymbol{u}}_j(\boldsymbol{X}) \exp(\mathrm{i}2\pi f_j t) + \text{c.c.} \tag{3.3a}$$

$$= \sum_{j=1}^{\infty} \sum_{k=1}^{M} a_j^{(k)} \boldsymbol{\Phi}_j^{(k)}(\boldsymbol{X}) \exp(\mathrm{i}2\pi f_j t) + \text{c.c.}, \tag{3.3b}$$

where $\mathrm{i} \equiv \sqrt{-1}$ and c.c. means the complex conjugate counterpart. Here, (3.3*a*) is the Fourier transform of the velocity field exploiting the homogeneity in time. In practice, the Fourier transform is performed employing Welch's overlapped window technique (Welch 1967), allowing multiple realizations for ensemble average. In (3.3*b*), the field of the Fourier-transformed coefficient for the jth frequency $\hat{\boldsymbol{u}}_j(\boldsymbol{X})$ is further decomposed into POD modes using singular value decomposition (SVD), in analogy to the space-only POD (see Meyer, Pedersen & Özcan 2007; Fang & Tachie 2019*b*). In (3.3*b*), $M = 200$ is the number of POD modes, which is determined by the number of windows of the Fourier transformation. Additionally, $\boldsymbol{\Phi}_j^{(k)}(\boldsymbol{X})$ represents the kth POD mode for the jth frequency, and its corresponding coefficient is denoted by $a_j^{(k)}$. The POD modes are orthonormal to each other, i.e. $\boldsymbol{\Phi}_j^{(p)}(\boldsymbol{X})[\boldsymbol{\Phi}_j^{(q)}(\boldsymbol{X})]^{\mathrm{T}} = \delta_{pq}$ (where superscript $^{\mathrm{T}}$ is the complex conjugate transpose, and the summation convention is not implied), so $\lambda_j^{(k)} \equiv |a_j^{(k)}|^2$ measures the

contribution of $\boldsymbol{\Phi}_j^{(k)}(\boldsymbol{X})$ to the integration of in-plane turbulence kinetic energy (E) over the analysed area. The rank of POD mode is thus arranged in descending order according to its energy $\lambda_j^{(k)}$. In essence, each SPOD mode represents a spatial structure varying over a designated temporal period (i.e. reciprocal of the corresponding frequency) described by

$$\boldsymbol{\Xi}_j^{(k)}(\boldsymbol{X}, \alpha) \equiv \boldsymbol{\Phi}_j^{(k)}(\boldsymbol{X}) \exp(\mathrm{i}2\pi f_j t) + \text{c.c.}, \tag{3.4}$$

where $\alpha \equiv 2\pi f_j t$ defines the phase angle.

We perform SPOD for the entire measurement area for all three test cases. Figure 15 compares the premultiplied frequency spectra of the first two SPOD modes. In general, for low frequencies (say $St_h < 0.2$), the energies held by the first modes are much higher than those by the second modes. This emphasizes the coherency of turbulent motions (or 'low-rank behaviour' as termed by Schmidt *et al.* 2018) at these low frequencies. In view of this, attention is limited to the first modes in the subsequent analyses. As mentioned earlier, the significant frequencies from the preceding discussions are summarized in table 1. As seen in figure 15(*a*) and table 1 for the smooth case, three dominant frequencies of similar energy levels are noted (i.e. $St_h = 0.050$, 0.089 and 0.115). These three frequencies have been identified using the velocity spectra in the mean shear layer, while the first two frequencies (i.e. $St_h = 0.050$ and 0.089) have also been identified in the region close to the mean reattachment point and in the instantaneous shear layer interface. As for the two rough cases, the dominant frequencies of the first SPOD modes do not always manifest in the aforementioned localized indicators. This suggests that either strong vortical structures do not necessarily exert strong influence everywhere, or some weak vortical structures are in fact locally dominant. The latter is exactly the situation with the flapping motion in the first half of the mean separation bubble, since in none of the cases does SPOD identify the low frequency corresponding to the flapping motion. It is also important to note from table 1 and figure 12 that the dominant frequencies close to the mean reattachment point in the near-wall region (at $y/h = -0.09$) for different test cases are fairly close to each other ($St_h \approx 0.09$). Therefore, the vortex shedding motion at a frequency higher than $St_h \approx 0.09$ is detached from the wall, whereas that at a frequency lower than $St_h \approx 0.09$ is touching the wall.

Figure 16 compares the first POD modes at the frequencies $St_h = 0.115$, 0.115 and 0.127 for the smooth, sandpaper and cube roughness cases, respectively. These plots are representative of significant frequencies higher than $St_h \approx 0.09$ identified in figure 15 for different cases, and are used to examine the vortical structures that are detached from the wall. Figure 16 shows Ξ (see (3.4)) at an arbitrary phase angle α, while supplementary movie 1 available at https://doi.org/10.1017/jfm.2022.661 shows the complete period of these SPOD modes, with α varying from 0 to 2π. In general, these modes exhibit consecutive slanted patches of alternating positive and negative streamwise fluctuating velocity. The inclination angles of these patches are about 45° regardless of the wall roughness conditions. This angle (45°) is the same as the angle of vortical structures conditioned on the wall pressure at the mean reattachment point observed by Kiya & Sasaki (1983, 1985). Within the streamwise range of the mean separation bubble, each slanted patch possesses two local peaks that are well separated by the isopleth of $U = 0$, and the upper peak is stacked over the lower peak of the adjacent downstream patch. As seen in supplementary movie 1 for figure 16, a train of vortices moves in the downstream direction in the close vicinity of the isopleth of $U = U_\infty$, and is attributed to the vortex shedding motion that originated in the separated shear layer. (An animation of the first

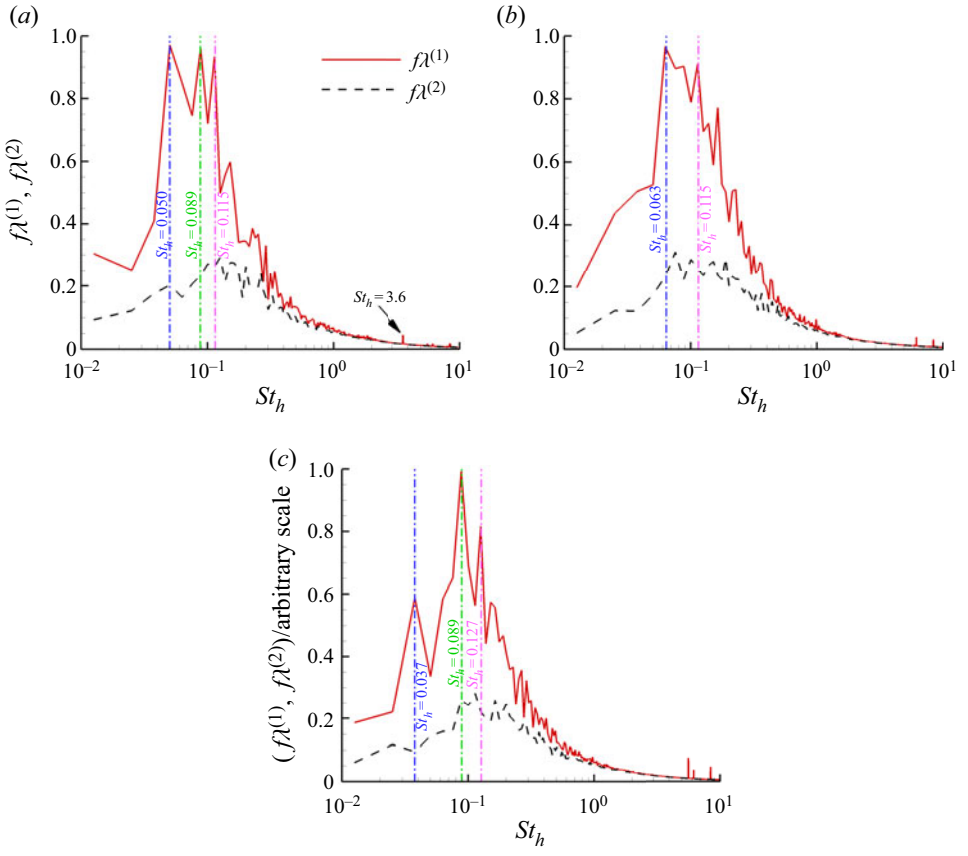

Figure 15. Premultiplied frequency spectra of the first and second SPOD modes ($f\lambda^{(1)}$ and $f\lambda^{(2)}$, respectively) for the (*a*) smooth, (*b*) sandpaper, and (*c*) cube roughness cases. The vertical dash-dotted lines mark characteristic frequencies of the first mode. The vertical axes use arbitrary scales.

SPOD mode at $St_h = 3.6$ for the smooth case is also supplied as supplementary movie 2; it signifies the vortical structures associated with the KH instability.)

In figure 16, two opposite-signed vortices (marked as A_1 and A_2) are centred on the isopleth of $U = 0$, while the vortex B_1 is centred on the isopleth of $U = U_\infty$. (For clarity, vortices centred on the isopleths of $U = 0$ and $U = U_\infty$ are named as A_i and B_i, respectively, where subscript i indicates the order of appearance in discussion.) Vortex B_1 is the first vortex shed in the separated shear layer at this frequency. The onset of each shed vortex goes through the following process. Vortices A_1 and B_1 are counter-rotating, consequently strong mode velocities are induced in between. This strong mode velocity also forms as an upstream part of vortex A_2. As the phase angle increases, vortices A_2 and B_1 are convected downstream while growing in size and maintaining their relative streamwise locations. Downstream of the mean reattachment point, however, only vortex B_1 (and its successors) remains. Meanwhile, alternating-signed vortices (see A_3 and A_4 in supplementary movie 1) appear along the frontal half of the isopleth of $U = 0$. As vortex A_1 is convected to beyond the mid-point of the mean reattachment length, vortex B_2 appears. The above process repeats itself except that the newly formed vortices are of opposite signs with their predecessors at the same locations. This process

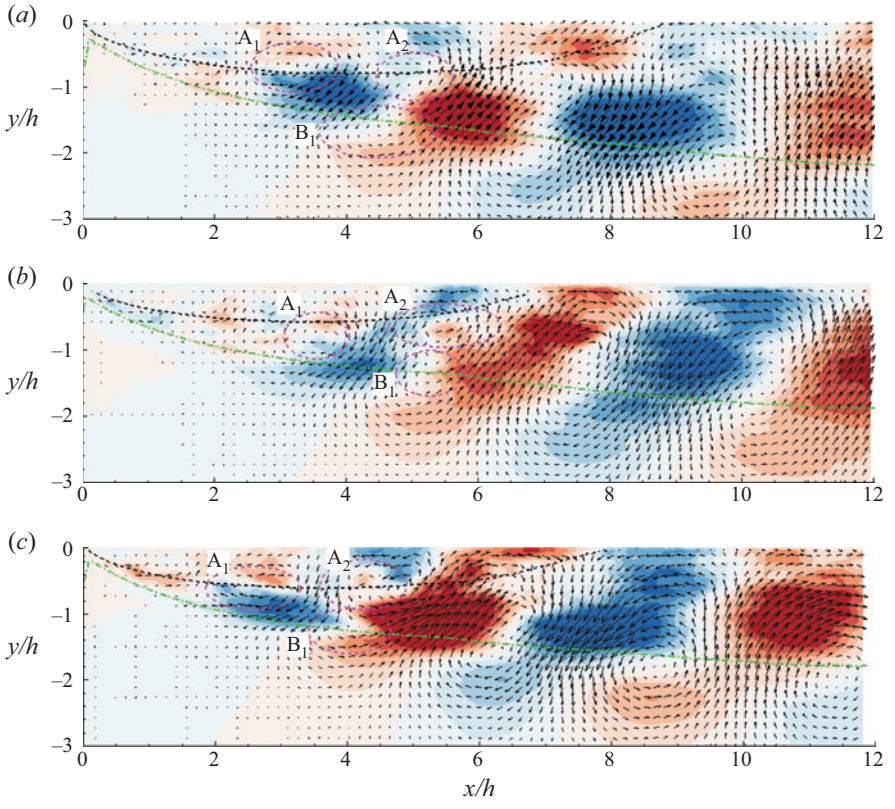

Figure 16. The first POD mode at (*a*) $St_h = 0.115$ for the smooth case, (*b*) $St_h = 0.115$ for the sandpaper case, and (*c*) $St_h = 0.127$ for the cube roughness case, at an arbitrary phase angle. The dashed and dash-dotted isopleths are at $U = 0$ and $U = U_\infty$, respectively. Blue and red indicate negative and positive streamwise velocity, respectively. Dashed ellipses mark characteristic vortices. An animated version is also provided as supplementary movie 1.

clearly demonstrates that the vortical structures encompassing the flow reversal are linked dynamically to the vortex shedding in the separated shear layer. By multiplying the wavelength with the corresponding mode frequency, the pertinent convective velocity of the vortex shedding shown in figure 16 is estimated to be approximately $0.6U_\infty$, which is close to the convective velocity of vortex shedding ($0.5U_\infty$) reported by Kiya & Sasaki (1983, 1985).

Figure 17 along with supplementary movie 3 examines the first POD modes at $St_h = 0.089$ for the three cases. Similar to figure 16, figure 17 reveals that the similar evolution process of alternating-signed vortices moving along the isopleths of $U = 0$ and $U = U_\infty$. This demonstrates that multiple vortex shedding motions at different frequencies are nested with the vortex cores aligned along the isopleth of $U = U_\infty$ in the separated shear layer. This conclusion is also in line with the deduction from § 3.2.1 that the instantaneous shear layer is bounded primarily by the isopleth of $u = U_\infty$. By comparing figures 16 and 17 along with supplementary movies 1 and 3, the variations of the vortical structures at lower frequencies are summarized as follows. The interaction of vortices A_i and B_i occurs in the more downstream locations, while the sizes of all visible vortices downstream of the mean reattachment point are larger. The elevated mode velocity of the vortices is closer to the wall. This explains why the dominant frequencies of $St_h \approx 0.09$ at

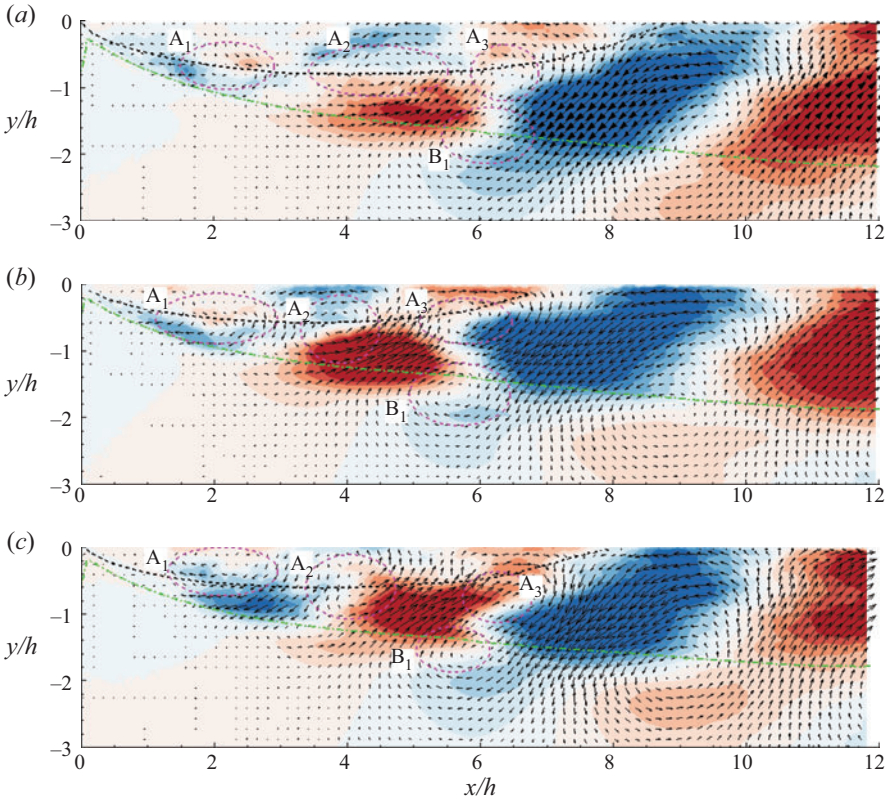

Figure 17. The first POD mode at (*a*) $St_h = 0.089$ for the smooth case, (*b*) $St_h = 0.089$ for the sandpaper case, and (*c*) $St_h = 0.089$ for the cube roughness case, at an arbitrary phase angle. The dashed and dash-dotted isopleths are at $U = 0$ and $U = U_\infty$, respectively. Blue and red indicate negative and positive streamwise velocity, respectively. Dashed ellipses mark characteristic vortices. See also supplementary movie 3.

$y/h = -0.09$ manifest near the mean reattachment point for all test cases (see figure 12). Additionally, strong mode velocity occurs between the isopleths of $U = 0$ and $U = U_\infty$, while new vortices (see A_3 and A_4 in supplementary movies 1 and 3) appear near the leading edge. The vortices A_i near flow reversal in the cube roughness case are closer to the wall than those in the other two cases. This is attributed to the distortion of the near-wall side of the vortex by the wall roughness. The wavelength of vortex shedding motion in the second half of the mean separation bubble is approximately $6h$ for all test cases, and the pertinent convective velocity is estimated to be $0.5U_\infty$. The vortices downstream of the mean reattachment point are deformed by the wall and exhibit longer characteristic wavelength than those in the second half of the mean separation bubble.

Figure 18 compares the first SPOD modes at the only significant frequencies lower than $St = 0.089$ in different test cases (see figure 15). As seen in figure 18(*a*) for the smooth case, the first vortex in the separated shear layer (near the isopleth of $U = U_\infty$) appears near the mean reattachment length. On the other hand, vortices along the isopleth of $U = 0$ occur with larger sizes and further downstream locations than those in figures 16 and 17. The supplementary movie (4) for figure 18(*a*) shows that as the phase angle increases, vortex A_2 approaches the mean reattachment point, and its vortex core becomes discernible while a vortex appears around $x/h = 7$ on the isopleth of $U = U_\infty$.

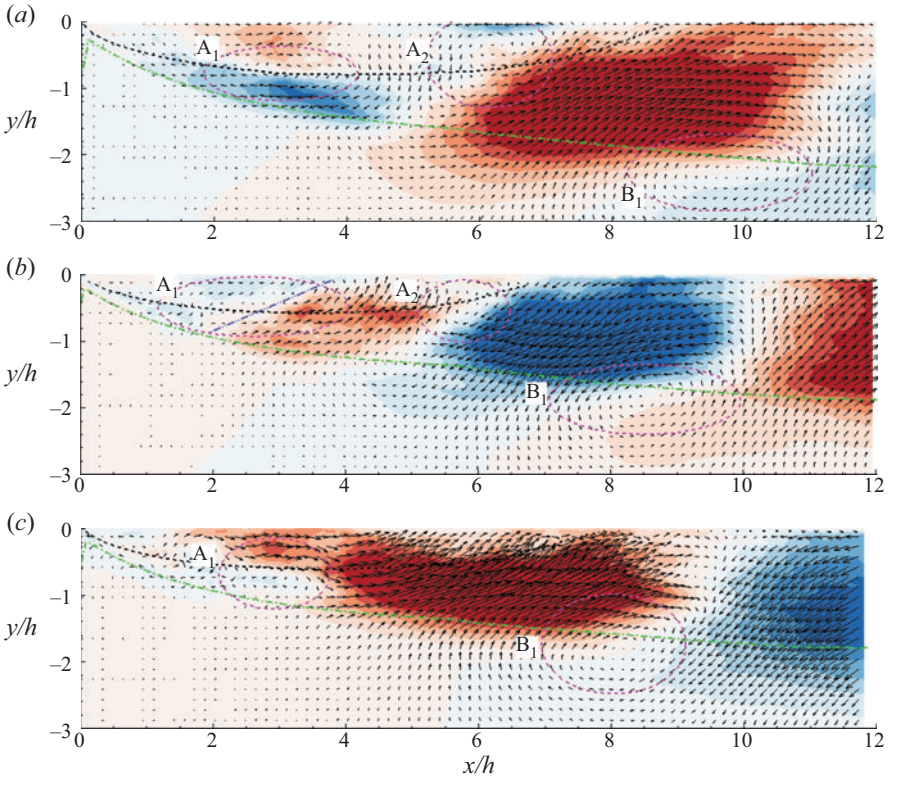

Figure 18. The first POD mode at (*a*) $St_h = 0.050$ for the smooth case, (*b*) $St_h = 0.063$ for the sandpaper case, and (*c*) $St_h = 0.037$ for the cube roughness case, at an arbitrary phase angle. The dashed and dash-dotted isopleths are at $U = 0$ and $U = U_\infty$, respectively. Blue and red indicate negative and positive streamwise velocity, respectively. Dashed ellipses mark characteristic vortices. See also supplementary movie 4.

Meanwhile, vortex A_2 grows larger, and a pair of counter-rotating vortices (A_2 and B_1) appears in the second half of the mean separation bubble. This process emphasizes that a vortex in the separated shear layer is always accompanied with an opposite-signed vortex in the area of mean flow reversal.

By comparing figures 18(*b*,*c*) with figure 18(*a*), it is evident that wall roughness exerts significant influence on the vortical structures at these low frequencies. In both rough cases, the pattern of a pair of counter-rotating vortices, one on the isopleth of $U = U_\infty$, and the other near the wall, are still visible. In the sandpaper case, vortex A_1 near the leading edge is inclined at a noticeable angle (see the dash-dot-dotted line in figure 18*b*) with the isopleth of $U = 0$, whereas that in the smooth case is aligned (measured by the interface where the streamwise mode velocity changes sign) tangential with the isopleth of $U = 0$. The orientation of vortex A_1 in the smooth case induces a near-wall area of elevated streamwise velocity that extends parallel with the wall, so that this lower part of the vortex is directly exposed to wall resistance. The orientation of vortex A_1 in the sandpaper, on the other hand, helps to move the location of elevated streamwise velocity away from the rough wall, thereby minimizing the contact length. This reduces the distortion of the vortex by wall roughness, so that the structure presented in figure 18(*b*) for the sandpaper case is survived. As seen in figure 18(*c*) and supplementary movie 4 for the cube roughness case,

vortex A_i is barely convected downstream and is destroyed abruptly, while the patch of negative/positive streamwise mode velocity downstream of it grows larger.

The results shown in figures 16, 17 and 18 can also provide some clarification to the well-recognized feedback influence of vortex shedding in flow separations. As commented by Bradshaw & Wong (1972): 'A key feature of the flow is found to be the splitting of the shear layer at reattachment, where part of the flow is deflected upstream into the recirculating flow region to supply the entrainment; the part of the flow that continues downstream suffers a pronounced decrease in eddy length scale, evidently because the larger eddies are torn in two'. A similar idea was adopted by Cimarelli *et al.* (2018), where they further concluded that the upstream convection of structures by the mean flow reversal contributes to a disturbance deflected upstream near the separating point. The results in figures 16, 17 and 18 suggest that the feedback influence of vortex shedding does exist, but it does not require any vortical structures to be convected upstream. In figure 16, the mode velocities flanked by vortices A_1 and B_1 are amplified, while vortex A_1 is convected downstream. In figures 17 and 18(*a*,*b*), vortex A_1 further induces another vortex in its upstream location in the mean flow reversal area, and generates elevated mode velocity in the channel flanked by the isopleths of $U = 0$ and $U = U_\infty$. As such, the process of vortex shedding in the separated shear layer is accompanied with patch(es) of intensified fluctuating velocities flanked by the isopleths of $U = 0$ and $U = U_\infty$ upstream of it. The patch(es) is(are) perhaps what Bradshaw & Wong (1972) referred to as 'part of the flow is deflected upstream'. The patches indeed 'supply the entrainment' due to the strong mode velocities deflected towards the flow separation at the interfaces.

The aforementioned feedback influence of vortex shedding is more significant for lower frequencies (especially $St_h < 0.09$) and is sensitive to the wall roughness condition. From figure 9, it is seen that the vortex shedding motion at the lower frequency ($St_h = 0.050$) in the smooth case exerts influence on the shear layer interface in more upstream locations than that at the higher frequency ($St_h = 0.089$). In contrast, the vortex shedding motions at lower frequencies in the rough cases do not manifest in the first half of the mean separation bubble. This is because the vortices near the mean flow reversal area are destroyed by the wall roughness, so that the feedback influence of vortex shedding is interrupted.

To investigate the underlying mechanism of flapping motion, figure 19 and supplementary movie 5 present the first SPOD mode at the dominant frequency of reverse flow areas in the first half of the mean separation bubble for different cases (figure 14). The flapping motion represents a low-frequency large-scale structure encompassing the entire separation bubble. This structure is relatively weak compared to the vortex shedding motions in the separated shear layer, thus its frequency does not manifest as local peaks in the SPOD spectra (figure 15). However, in the first half of the mean separation bubble, where the turbulence intensity induced by the vortex shedding motions is relatively weak, this large-scale structure, although weak, is influential and manifests as a low-frequency oscillation of reverse flow areas (figure 14). From the supplementary movie (5) for figure 19, for all test cases, a vortex appears in the area of mean flow reversal, and is subsequently deflected away from the mean separation bubble downstream of the mean reattachment point. The flapping motion of flow separation thus reflects the alteration of reverse flow area by the accompanied fluctuating velocity of vortices. This analysis is consistent with the deduction by Kiya & Sasaki (1983) that the low-frequency flapping motion leads to an abrupt shedding of an extremely large vortex from flow separation. A similar conclusion was made by Hillier & Cherry (1981), Tafti & Vanka (1991) and Yang & Voke (2001).

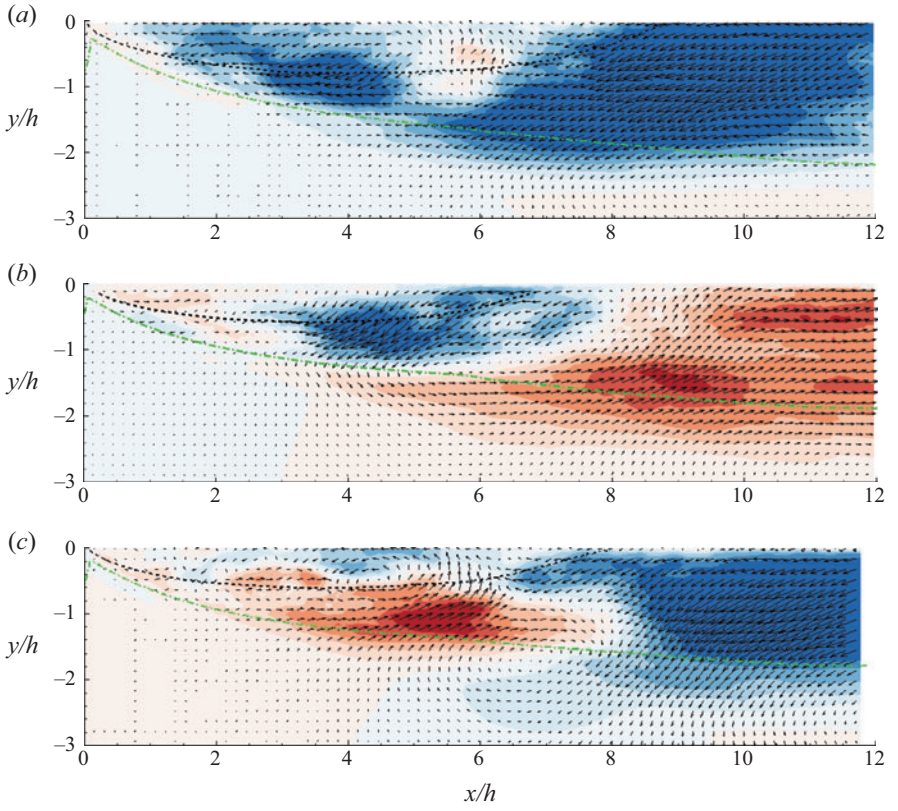

Figure 19. The first POD mode at (*a*) $St_h = 0.025$ for the smooth case, (*b*) $St_h = 0.025$ for the sandpaper case, and (*c*) $St_h = 0.050$ for the cube roughness case, at an arbitrary phase angle. The dashed and dash-dotted isopleths are at $U = 0$ and $U = U_\infty$, respectively. Blue and red indicate negative and positive streamwise velocity, respectively. See also supplementary movie 5.

4. Summary and conclusions

The spatio-temporal characteristics of flow separations beneath a semi-submerged bluff body with varying undersurface roughness conditions are studied using time-resolved particle image velocimetry. Two different wall roughness conditions, consisting of sandpaper and cube roughness as well as a reference smooth wall, are examined. The Reynolds number based on the free-stream velocity and submergence depth is 14 400. This Reynolds number is close to those based on half body height examined by Kiya & Sasaki (1983, 1985) and Moore *et al.* (2019) for bluff bodies subjected to incoming uniform flows. The free-stream turbulence intensity is about 1.3 %, and the Froude number is 0.23. As such, the free surface is free of waves, and is analogous to the centreline symmetry plane of a bluff body immersed in uniform flows.

Beneath the bluff bodies, the mean flow separates at the leading edge and reattaches on the undersurface, forming a mean recirculation bubble. When properly scaled, the mean reattachment length in the smooth case is similar to values reported for bluff bodies immersed in uniform flows at comparable Reynolds numbers. Wall roughness reduces the mean reattachment length and the maximum magnitude of mean flow reversal by approximately 16–20 % and 18 %, respectively. Wall roughness also reduces the Reynolds stresses in the second half of the mean separation bubble. The instantaneous shear layer is

primarily confined by the isopleth of $u = U_\infty$. The convolution of the probability density function of this isopleth and the conditional-averaged streamwise velocity in the vertical neighbourhood of this isopleth gives close approximation of the total streamwise Reynolds normal stress.

Near the leading edge, the Kelvin–Helmholtz instability occurs at $St_h = 3.6$ in the smooth case, but is bypassed in the rough cases. Upstream of the mid-point of mean reattachment length, the dominant frequencies in the separated shear layer migrate from high to low values in a discrete manner through the vortex pairing mechanism, which is at variance with the continuous spectra migration reported by Moore *et al.* (2019). In turn, multiple vortex shedding motions at different frequencies are nested along the isopleth of $U = U_\infty$. Each vortex shedding motion initiates as an interaction between vortices centred on the isopleths of $U = 0$ and $U = U_\infty$. The vortex shedding motions at $St_h > 0.090$ are detached from the wall, thus are not affected significantly by the wall roughness conditions. The vortex shedding motions at $St_h < 0.090$, on the other hand, interact directly with the wall, and are susceptible to wall roughness conditions. In particular, in the smooth case, the vortex shedding motion at $St_h < 0.090$ generates a strong flux of streamwise fluctuating velocity channelled between the isopleths of $U = 0$ and $U = U_\infty$ near the leading edge. This channelled fluctuating velocity near the leading edge becomes stronger as the shed vortices are convected downstream along the isopleth of $U = U_\infty$. This creates an illusion that the influence of vortex shedding motion in the downstream location is fed back to the upstream location, which has been conjectured previously by Bradshaw & Wong (1972) and Kiya & Sasaki (1985). This feedback influence is disrupted by the wall roughness.

There exists a low-frequency structure that imposes negative/positive streamwise fluctuating velocity over the entire mean separation bubble. This structure modulates the reverse flow area, creating a flapping motion of separated shear layer. The frequency of flapping motion is identified as the dominant frequency of reverse flow area in the first half of the mean separation bubble. The flapping motions in the smooth and sandpaper cases are at a similar frequency $St_h = 0.025$, but lower than $St_h = 0.050$ in the cube roughness case. During the switching of negative and positive streamwise fluctuating velocity at this low frequency, a vortex appears suddenly around the mean reattachment point, and then moves quickly towards a downstream direction away from the wall before disappearing outside the isopleth of $U = U_\infty$.

Supplementary movies. Supplementary movies are available at https://doi.org/10.1017/jfm.2022.661.

Funding. We gratefully acknowledge the financial support from Manitoba Hydro and Natural Sciences and Engineering Research Council (NSERC) of Canada Alliance and Discovery Grants. We are also grateful to Canada Foundation for Innovation (CFI) for providing funding for the experimental facility.

Declaration of interests. The authors report no conflict of interest.

Author ORCIDs.
Xingjun Fang https://orcid.org/0000-0003-2005-7269;
Mark F. Tachie https://orcid.org/0000-0002-0385-1391.

References

Adrian, R.J., Meinhart, C.D. & Tomkins, C.D. 2000 Vortex organization in the outer region of the turbulent boundary layer. *J. Fluid Mech.* **422**, 1–54.

Ashton, G.D. 1974 Froude criterion for ice-block stability. *J. Glaciol.* **13** (68), 307–313.

Bai, H. & Alam, Md.M. 2018 Dependence of square cylinder wake on Reynolds number. *Phys. Fluids* **30**, 015102.

BRADSHAW, P. & WONG, F.Y.F. 1972 The reattachment and relaxation of a turbulent shear layer. *J. Fluid Mech.* **52** (1), 113–135.

BRUN, C., AUBRUN, S., GOOSSENS, T. & RAVIER, PH. 2008 Coherent structures and their frequency signature in the separated shear layer on the sides of a square cylinder. *Flow Turbul. Combust.* **81**, 97–114.

CASTRO, I.P. & HAQUE, A. 1987 The structure of a turbulent shear layer bounding a separation region. *J. Fluid Mech.* **179**, 439–468.

CHALMERS, H.A., FANG, X. & TACHIE, M.F. 2021 Streamwise aspect ratio effects on turbulent flow separations induced by forward–backward-facing steps. *Trans. ASME J. Fluids Engng* **143**, 021305.

CHERRY, N.J., HILLIER, R. & LATOUR, M.E.M.P. 1984 Unsteady measurements in a separated and reattaching flow. *J. Fluid Mech.* **144**, 13–46.

CHIARINI, A., QUADRIO, M. & AUTERI, F. 2022 On the frequency selection mechanism of the low-*Re* flow around rectangular cylinders. *J. Fluid Mech.* **933**, A44.

CIMARELLI, A., LEONFORTE, A. & DE ANGELI, E. 2018 On the structure of the self-sustaining cycle in separating and reattaching flows. *J. Fluid Mech.* **857**, 907–936.

COUTERMARSH, B. & MCGILVARY, W.R. 1993 Static analysis of floating ice block stability. *J. Hydraul. Res.* **31** (2), 147–160.

DE SILVA, C.M., HUTCHINS, N. & MARUSIC, I. 2016 Uniform momentum zones in turbulent boundary layers. *J. Fluid Mech.* **786**, 309–331.

DE SILVA, C.M., PHILIP, J., HUTCHINS, N. & MARUSIC, I. 2017 Interfaces of uniform momentum zones in turbulent boundary layers. *J. Fluid Mech.* **820**, 451–478.

DJILALI, N. & GARTSHORE, I.S. 1991 Turbulent flow around a bluff rectangular plate. Part I: experimental investigation. *Trans. ASME J. Fluids Engng* **113** (1), 51–59.

DOW AMBTMAN, K.E., STEFFLER, P.M. & HICKS, F.E. 2011*a* Analysis of the stability of floating ice blocks. *J. Hydraul. Engng ASCE* **137** (4), 412–422.

DOW AMBTMAN, K.E., STEFFLER, P.M. & HICKS, F.E. 2011*b* Experimental investigation of the pressure distribution beneath a floating ice block. *J. Hydraul. Engng ASCE* **137** (4), 399–411.

DURÃO, D.F.G., HEITOR, M.V. & PEREIRA, J.C.F. 1988 Measurements of turbulent and periodic flows around a square cross-section cylinder. *Exp. Fluids* **6**, 298–304.

EATON, J.K. & JOHNSTON, J.P. 1981 A review of research on subsonic turbulent flow reattachment. *AIAA J.* **19**, 1093–1100.

EATON, J.K. & JOHNSTON, J.P. 1982 Low frequency unsteadiness of a reattaching turbulent shear layer. In *Turbulent Shear Flows* (ed. L.J.S. Bradbury, F. Durst, B.E. Launder, F.W. Schmidt & J.H. Whitelaw), vol. 3, pp. 162–170.

ESSEL, E.E., NEMATOLLAHI, A., THACHER, E.W. & TACHIE, M.F. 2015 Effects of upstream roughness and Reynolds number on separated and reattached turbulent flow. *J. Turbul.* **16** (9), 872–899.

ESSEL, E.E. & TACHIE, M.F. 2015 Roughness effects on turbulent flow downstream of a backward facing step. *Flow Turbul. Combust.* **94** (1), 125–153.

ESSEL, E.E. & TACHIE, M.F. 2017 Upstream roughness and Reynolds number effects on turbulent flow structure over forward facing step. *Intl J. Heat Fluid Flow* **66**, 226–242.

ESSEL, E.E., TACHIE, M.F. & BALACHANDAR, R. 2021 Time-resolved wake dynamics of finite wall-mounted circular cylinders submerged in a turbulent boundary layer. *J. Fluid Mech.* **917**, A8.

FANG, X., DOW, K., TACHIE, M.F., MALENCHAK, J. & WANG, S. 2022 Flow characteristics beneath ice blocks with smooth and rough undersurfaces. *J. Hydraul. Engng ASCE* (submitted).

FANG, X. & TACHIE, M.F. 2019*a* Flows over surface-mounted bluff bodies with different spanwise widths submerged in a deep turbulent boundary layer. *J. Fluid Mech.* **877**, 717–758.

FANG, X. & TACHIE, M.F. 2019*b* On the unsteady characteristics of turbulent separations over a forward–backward-facing step. *J. Fluid Mech.* **863**, 994–1030.

FANG, X. & TACHIE, M.F. 2020 Spatio-temporal dynamics of flow separation induced by a forward-facing step submerged in a thick turbulent boundary layer. *J. Fluid Mech.* **892**, A40.

FANG, X., TACHIE, M.F., BERGSTROM, D.J., YANG, Z. & WANG, B.-C. 2021 Three-dimensional structural characteristics of flow separation induced by a forward-facing step in a turbulent channel flow. *J. Fluid Mech.* **919**, A24.

GRAZIANI, A., KERHERVÉ, F., MARTINUZZI, R.J. & KEIRSBULCK, L. 2018 Dynamics of the recirculating areas of a forward-facing step. *Exp. Fluids* **59**, 154.

HATTORI, H. & NAGANO, Y. 2010 Investigation of turbulent boundary layer over forward-facing step via direct numerical simulation. *Intl J. Heat Fluid Flow* **31** (3), 284–294.

HEARST, R.J., GOMIT, G. & GANAPATHISUBRAMANI, B. 2016 Effect of turbulence on the wake of a wall-mounted cube. *J. Fluid Mech.* **804**, 513–530.

HILLIER, R. & CHERRY, N.J. 1981 The effects of stream turbulence on separation bubbles. *J. Wind Engng Ind. Aerodyn.* **8**, 49–58.
HO, C.-M. & HUERRE, P. 1984 Perturbed free shear layers. *Annu. Rev. Fluid Mech.* **16**, 365–424.
KIVISILD, H.R. 1959 Hanging ice dams. In *Proceedings of the 8th Congress of the International Association for Hydraulic Research*, vol. 2, pp. 1–30.
KIYA, M. & SASAKI, K. 1983 Structure of a turbulent separation bubble. *J. Fluid Mech.* **137**, 83–113.
KIYA, M. & SASAKI, K. 1985 Structure of large-scale vortices and unsteady reverse flow in the reattaching zone of a turbulent separation bubble. *J. Fluid Mech.* **154**, 463–491.
KUMAHOR, S. & TACHIE, M.F. 2022 Turbulent flow around rectangular cylinders with different streamwise aspect ratios. *Trans. ASME J. Fluids Engng* **144** (5), 051304.
LANDER, D.C., LETCHFORD, C.W., AMITAY, M. & KOPP, G.A. 2016 Influence of the bluff body shear layers on the wake of a square prism in a turbulent flow. *Phys. Rev. Fluids* **1**, 044406.
LANDER, D.C., MOORE, D.M., LETCHFORD, C.W. & AMITAY, M. 2018 Scaling of square-prism shear layers. *J. Fluid Mech.* **849**, 1096–1119.
LASKARI, A., DE KAT, R., HEARST, R.J. & GANAPATHISUBRAMANI, B. 2018 Time evolution of uniform momentum zones in a turbulent boundary layer. *J. Fluid Mech.* **842**, 554–590.
LEGRAND, M., NOGUEIRA, J. & LECUONA, A. 2011 Flow temporal reconstruction from non-time-resolved data part I: mathematic fundamentals. *Exp. Fluids* **51**, 1047–1055.
LYN, D.A. & RODI, W. 1995 A laser-Doppler velocimetry study of ensemble-averaged characteristics of the turbulent near wake of a square cylinder. *J. Fluid Mech.* **304**, 285–319.
MEYER, K.E., PEDERSEN, J.M. & ÖZCAN, O. 2007 A turbulent jet in crossflow analysed with proper orthogonal decomposition. *J. Fluid Mech.* **583**, 199–227.
MOHAMMED-TAIFOUR, A. & WEISS, J. 2016 Unsteadiness in a large turbulent separation bubble. *J. Fluid Mech.* **799**, 383–412.
MOORE, D.W., LETCHFORD, C.W. & AMITAY, M. 2019 Energetic scales in a bluff body shear layer. *J. Fluid Mech.* **875**, 543–575.
NAKAGAWA, S., SENDA, M., KIKKAWA, S., WAKASUGI, H. & HIRAIDE, A. 1998 Heat transfer in channel flow around a rectangular cylinder. *Heat Transfer Japan Res.* **27** (1), 84–97.
NEMATOLLAHI, A. & TACHIE, M.F. 2018 Time-resolved PIV measurement of influence of upstream roughness on separated and reattached turbulent flows over a forward-facing step. *AIP Adv.* **8**, 105110.
OKAJIMA, A. 1982 Strouhal number of rectangular cylinders. *J. Fluid Mech.* **123**, 379–398.
OTA, T., ASANO, Y. & OKAWA, J. 1981 Reattachment length and transition of the separated flow over blunt flat plates. *Bull. JSME* **24** (192), 941–947.
OTA, T. & ITASAKA, M. 1971 A separated and reattached flow on a blunt flat plate. *Trans. ASME J. Fluids Engng* **98** (1), 79–84.
OTA, T. & NARITA, M. 1978 Turbulence measurements in a separated and reattached flow over a blunt flat plate. *Trans. ASME J. Fluids Engng* **100**, 224–228.
VAN OUDHEUSDEN, B.W., SCARANO, F., VAN HINSBERG, N.P. & WATT, D.W. 2005 Phase-resolved characterization of vortex shedding in the near wake of a square-section cylinder at incidence. *Exp. Fluids* **39**, 86–98.
PARISET, E. & HAUSSER, R. 1961 Formation and evolution of ice covers on rivers. *Trans. Eng. Inst. Canada* **5** (1), 41–49.
PEARSON, D.S., GOULART, P.J. & GANAPATHISUBRAMANI, B. 2013 Turbulent separation upstream of a forward-facing step. *J. Fluid Mech.* **724**, 284–304.
PIIRTO, M., SAARENRINNE, P., ELORANTA, H. & KARVINEN, R. 2003 Measuring turbulence energy with PIV in a backward-facing step flow. *Exp. Fluids* **35** (3), 219–236.
POPE, S.B. 2000 *Turbulent Flows*. Cambridge University Press.
RAFFEL, M., WILLERT, C.E., WERELEY, S.T. & KOMPENHANS, J. 2007 *Particle Image Velocimetry*. Springer.
SAMIMY, M. & LELE, S. 1991 Motion of particles with inertia in a compressible free shear layer. *Phys. Fluids* A **3** (8), 1915–1923.
SASAKI, K. & KIYA, M. 1991 Three-dimensional vortex structure in a leading-edge separation bubble at moderate Reynolds numbers. *Trans. ASME J. Fluids Engng* **113** (3), 405–410.
SAXTON-FOX, T. & MCKEON, B.J. 2017 Coherent structures, uniform momentum zones and the streamwise energy spectrum in wall-bounded turbulent flow. *J. Fluid Mech.* **826**, R6.
SCHMIDT, O.T., TOWNE, A., RIGAS, G., COLONIUS, T. & BRÈS, G.A. 2018 Spectral analysis of jet turbulence. *J. Fluid Mech.* **855**, 953–982.
SCIACCHITANO, A. & WIENEKE, B. 2016 PIV uncertainty propagation. *Meas. Sci. Technol.* **27** (8), 84006.

SHERRY, M., LO JACONO, D. & SHERIDAN, J. 2010 An experimental investigation of the recirculation zone formed downstream of a forward facing step. *J. Wind Engng Ind. Aerodyn.* **98** (12), 888–894.

TAFTI, D.K. & VANKA, S.P. 1991 A three-dimensional numerical study of flow separation and reattachment on a blunt plate. *Phys. Fluids* A **3**, 2887–2909.

TOWNE, A., SCHMIDT, O.T. & COLONIUS, T. 2018 Spectral proper orthogonal decomposition and its relationship to dynamic mode decomposition and resolvent analysis. *J. Fluid Mech.* **847**, 821–867.

UZUNER, M.S. & KENNEDY, J.F. 1972 Stability of floating ice blocks. *J. Hydraul. Div. ASCE* **98** (HY12), 2117–2133.

WELCH, P. 1967 The use of fast Fourier transform for the estimation of power spectra: a method based on time averaging over short, modified periodograms. *IEEE Trans. Audio Electroacoust.* **15** (2), 70–73.

WESTERWEEL, J., FUKUSHIMA, C., PEDERSEN, J.M. & HUNT, J.C.R. 2005 Mechanics of the turbulent–nonturbulent interface of a jet. *Phys. Rev. Lett.* **95**, 174501.

WINANT, C.D. & BROWAND, F.K. 1974 Vortex pairing: the mechanism of turbulent mixing-layer growth at moderate Reynolds number. *J. Fluid Mech.* **63** (2), 237–255.

YANG, Z. & VOKE, P.R. 2001 Large-eddy simulation of boundary-layer separation and transition at a change of surface curvature. *J. Fluid Mech.* **439**, 305–333.

ZHOU, J., ADRIAN, R.J., BALACHANDAR, S. & KENDALL, T.M. 1999 Mechanisms for generating coherent packets of hairpin vortices in channel flow. *J. Fluid Mech.* **387**, 353–396.